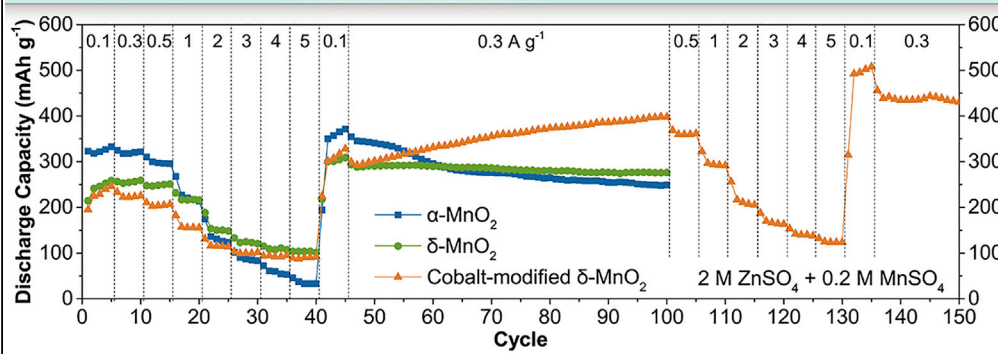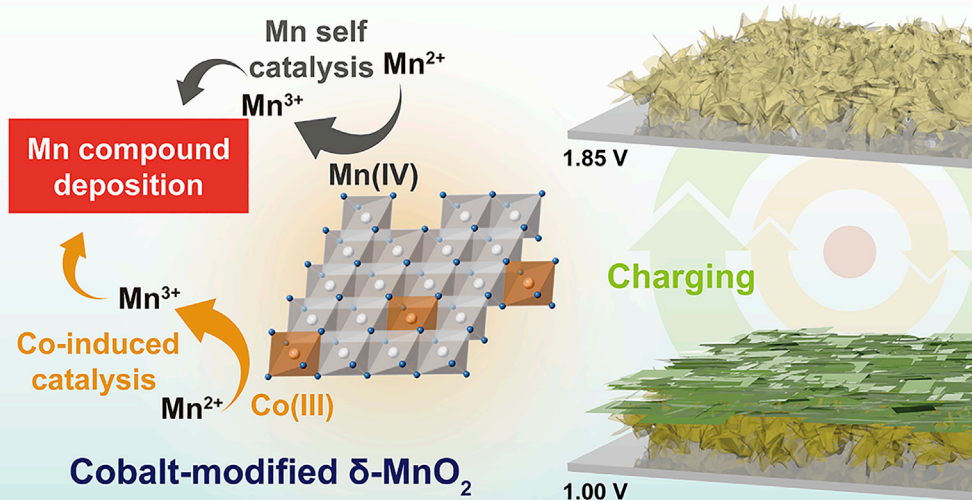Article

Self-Recovery Chemistry and Cobalt-Catalyzed Electrochemical Deposition of Cathode for Boosting Performance of Aqueous Zinc-Ion Batteries

Yijun Zhong, Xiaomin Xu, Jean-Pierre Veder, Zongping Shao

zongping.shao@curtin.edu.au

HIGHLIGHTS

Key factor of capacity retention: active Mn compound deposition rate

A novel cobalt-catalyzed deposition strategy and the dynamic cobalt movement

Excellent performance (>500 mAh g^{-1}) and retention (63%) over 5,000 cycles

Improvement of cycling stability with minimized Mn^{2+} additive

Article

Self-Recovery Chemistry and Cobalt-Catalyzed Electrochemical Deposition of Cathode for Boosting Performance of Aqueous Zinc-Ion Batteries

Yijun Zhong,[1] Xiaomin Xu,[1] Jean-Pierre Veder,[2] and Zongping Shao[1,3,4,*]

SUMMARY

Rechargeable Zn-ion batteries working with manganese oxide cathodes and mild aqueous electrolytes suffer from notorious cathode dissolution during galvanostatic cycling. Herein, for the first time we demonstrate the dynamic self-recovery chemistry of manganese compound during charge/discharge processes, which strongly determines the battery performance. A cobalt-modified δ-MnO_2 with a redox-active surface shows superior self-recovery capability as a cathode. The cobalt-containing species in the cathode enable efficient self-recovery by continuously catalyzing the electrochemical deposition of active Mn compound, which is confirmed by characterizations of both practical coin-type batteries and a new-design electrolyzer system. Under optimized condition, a high specific capacity over 500 mAh g^{-1} is achieved, together with a decent cycling performance with a retention rate of 63% over 5,000 cycles. With this cobalt-facilitated deposition effect, the battery with low concentration (0.02 M) of additive Mn^{2+} in the electrolyte (only 12 atom % to the overall Mn) maintains decent capacity retention.

INTRODUCTION

Since their first commercialization in the 1990s, rechargeable lithium-ion batteries (LIBs), which are characterized by high voltage, high energy density, and long cycling stability, have been widely used as portable power source in many aspects of our daily life during the past three decades, in particular in the field of personal electronics (Lin et al., 2017; Du et al., 2019; Zhao et al., 2015). The state-of-the-art LIBs use organic-based electrolytes, which, however, can introduce serious safety concerns for large-scale applications, such as electrochemical energy storage for electric grid and power source for electric vehicles (Hu and Xu, 2014). In addition, the limited resource of lithium also brings a big concern about the cost of LIBs when their widespread application is realized. Therefore, battery systems with higher safety and lower cost are highly demanded (Lukatskaya et al., 2016; Ming et al., 2019; Zhong et al., 2019; Lu et al., 2019). Compared with conventional organic electrolytes, inorganic, aqueous electrolytes usually have improved ionic conductivity, higher safety, and lower fabrication cost (Lu et al., 2011; Fang et al., 2018). Aqueous batteries based on different metal ions, e.g., Li$^+$, Na$^+$, Zn^{2+}, Mg^{2+}, and Al^{3+}, have been developed and intensively studied over the past decades (Luo et al., 2010; Li et al., 2015; Verma et al., 2019). In particular, zinc-ion (Zn-ion) batteries have attracted increasing attention owing to the abundance of Zn resource and the relatively high electrochemical potential of Zn metal in neutral or mildly acidic aqueous electrolytes, which is beneficial to the stable performance (Konarov et al., 2018; Song et al., 2018; Zeng et al., 2019). The concept and the fundamental chemistry of the rechargeable Zn-ion batteries based on the migration of Zn^{2+} between cathode and anode was first proposed by Kang and co-workers in 2011 (Xu et al., 2012; Li et al., 2019a). In recent years, intensive efforts have been made to the investigation of the composition of aqueous electrolytes, the preparation and protection of Zn anodes, and the development of high-performance and stable cathode materials (Zeng et al., 2019; Yang et al., 2019; Zhang et al., 2017).

Compared with metallic Zn anode, the capacity of the cathode is usually much lower, which becomes one of the bottlenecks for the commercialization of aqueous Zn-ion batteries. Till now, most of the research activities on Zn-ion batteries have been focused on the development and modification of the cathode. Transition metals with high valent states, e.g., Mn (Cheng et al., 2005; Xu et al., 2012; Alfaruqi et al., 2015; Pan et al., 2016, 2018; Zhang et al., 2016, 2017; Huang et al., 2018; Wu et al., 2018), V (Kundu et al., 2016, 2018; Wan et al., 2018; He et al., 2017; Yan et al., 2018; Wan and Niu, 2019), and Mo (Chae et al., 2016; Li

[1]WA School of Mines: Minerals, Energy and Chemical Engineering (WASM-MECE), Curtin University, Perth, WA 6845, Australia

[2]John de Laeter Centre, Curtin University, Perth, WA 6102, Australia

[3]State Key Laboratory of Materials-Oriented Chemical Engineering, College of Chemical Engineering, Nanjing Tech University, Nanjing, Jiangsu 210009, P.R. China

[4]Lead Contact

*Correspondence: zongping.shao@curtin.edu.au

https://doi.org/10.1016/j.isci.2020.100943

et al., 2019b; Kaveevivitchai and Manthiram, 2016), are more suitable cathode materials for Zn-ion batteries as a bivalent ion battery system, and therefore they have been widely studied (Verma et al., 2019). Actually, Zn/MnO_2 battery is one of the earliest systems for primary Zn-based batteries, which has achieved commercialization many years ago (Li et al., 2019a). Owing to the fast kinetics of Mn redox reactions, Mn compounds (e.g., MnO_2) show promising capability as high-performance cathodes for rechargeable Zn-ion batteries (Cheng et al., 2005; Pan et al., 2016; Ha and Lee, 2016). In recent years, a variety of modification strategies (e.g., pre-intercalation, heteroatom doping, and defect engineering) have been proposed for improving the performance of the Mn-based cathodes (Wang et al., 2019a; Long et al., 2019; Xiong et al., 2019; Fang et al., 2019). For example, pre-intercalation of ions or molecules (e.g., Na^+, Zn^{2+}, polyaniline or water) in the layered MnO_2 can boost the redox kinetics by facilitating the charge storage (Wang et al., 2019a, 2019b; Huang et al., 2018). Doping cathode materials with cobalt or nickel is beneficial to improve the energy density of the cathode by increasing the discharge voltage or improving the electronic conductivity (Long et al., 2019; Pan et al., 2018; Ma et al., 2019).

Despite significant advantages (e.g., high theoretical capacity, low cost, low toxicity), the notorious instability of the Mn-based cathodes during recharging cycles severely impedes their use in practical Zn-ion batteries (Nam et al., 2019; Fang et al., 2019). The instability could be mainly associated with the disproportionation of Mn(III), generating Mn(IV) and highly soluble Mn(II) (Song et al., 2018; Yu et al., 2019). It is important to note that for MnO_2, regardless of its initial phase structure (e.g., α-MnO_2, β-MnO_2, γ-MnO_2 or δ-MnO_2), this charge disproportionation is very likely to happen, leading to the same result of the dissolution and loss of active Mn compound and, consequently, deterioration of the capacity. To address this issue, additional Mn^{2+} at high concentrations (usually 0.1–0.5 M) was proposed to be introduced into the electrolyte to suppress the disproportionation reaction (Pan et al., 2016; Wu et al., 2018; Huang et al., 2018, 2019a, 2019b; Zhang et al., 2017; Fang et al., 2019). The cycling stability of Mn-based cathodes has been greatly enhanced by adopting this strategy. However, this enhancement is at the expense of reduced mass energy density of the battery, given that the large proportion of the extra Mn^{2+} occupies additional weight but might not provide decent capacity.

To date, mechanisms behind the enhanced stability of Zn-ion batteries with Mn^{2+}-containing electrolytes are still unclear. Recent reports have provided some clues that Mn^{2+} in the electrolyte can be oxidized, inducing the deposition of active Mn compound on the cathode surface (Gibson et al., 2016; Li et al., 2019c). This suggests that the deposition of Mn compound from the Mn^{2+}-containing electrolytes is also an important phenomenon that deserves more research attention. Such a self-recovery phenomenon resulting from the deposition of Mn compound on the cathode may have a significant effect on the capacity and stability of Zn-ion batteries. However, most of the previous reports evaluated the capacity only based on the weight of the Mn-based cathode. In addition, only the Mn^{2+} concentration in the electrolyte was given, whereas information about the volume of the electrolyte and the Mn ratio (atomic/weight) of the solid Mn-based cathode to the aqueous Mn^{2+} in the electrolyte is lacking. This could lead to an unreliable comparison of the results across different publications. Owing to the potential contribution of Mn^{2+} in the electrolyte to the capacity, retention rates of the cathode much higher than 100% were observed in some literature reports where the capacity was calculated just based on the active material at the cathode (Wu et al., 2018; Fu et al., 2018; Zhu et al., 2018; Wang et al., 2019b).

All these facts emphasize the motivation of this work, i.e., to study self-recovery chemistry in the cathode of Zn-ion batteries, including the influencing parameters for the process and their interactions and the mechanism behind the electrochemical deposition of Mn compound during the battery cycling. Based on the understanding of the self-recovery chemistry in the cathode, we further propose a cobalt-modified δ-MnO_2 as a cathode material with a redox-active surface for fast deposition of Mn compound. To emphasize the importance of the deposition rate of the Mn-active compounds for the self-recovery cycling capacity, an equation that describes the dynamic capacity of the Mn-based cathode is also demonstrated. The cobalt-induced facilitating of deposition is confirmed by the electrochemical and chemical characterizations of both practical coin-type batteries and a newly designed electrolyzer system. Insights into the catalysis routes of the Mn compound deposition are also revealed. This work provides guidance of the utility of the Mn^{2+}-containing electrolyte for the development of Zn-ion batteries and may provide inspiration for materials engineering for future functionalized cathodes, especially for other conversion-type battery cathodes, which have similar dissolution issues.
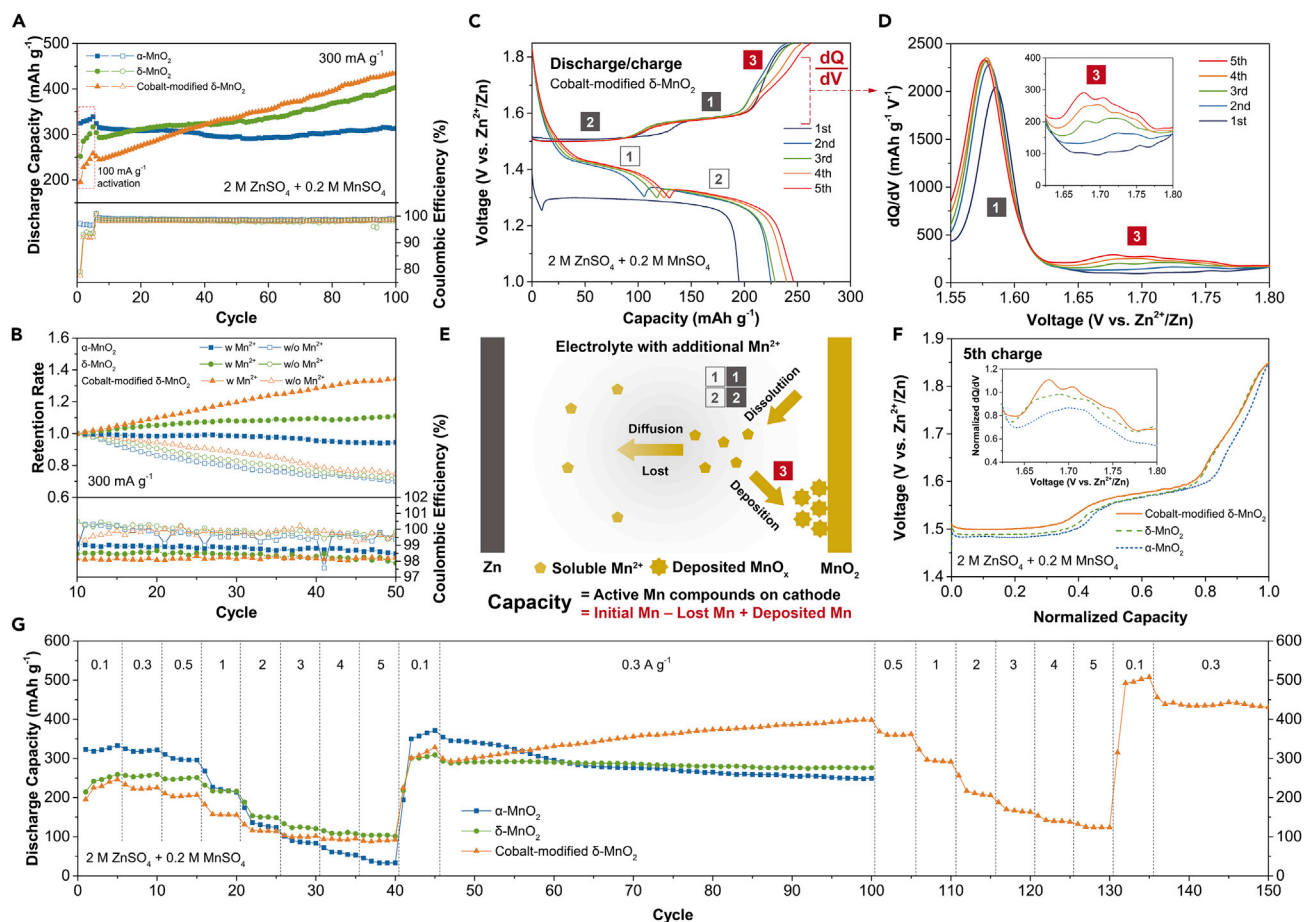
Figure 1. Comparison of Performance and the Self-Recovery Chemistry in a MnO₂ Cathode

(A) Comparison of cycling performance of α-MnO₂, δ-MnO₂, and cobalt-modified δ-MnO₂ cathodes with a 2 M ZnSO₄ electrolyte containing 0.2 M MnSO₄.

(B) Comparison of retention rates and Coulombic efficiencies of the MnO₂ cathodes with or without 0.2 M MnSO₄ in the electrolyte (the calculation of retention rate is based on the 10th discharging of the cathodes).

(C and D) (C) First five galvanostatic discharging and charging profiles of a cobalt-modified δ-MnO₂ cathode and (D) the corresponding dQ/dV profiles from 1.55 to 1.80 V.

(E) A schematic and an equation for describing the dynamic capacity retention of a Mn-based cathode.

(F) Comparison of the fifth charging of the MnO₂ cathodes; inset shows their corresponding dQ/dV profiles from 1.62 to 1.80 V.

(G) Comparison of the rate performance of α-MnO₂, δ-MnO₂, and cobalt-modified δ-MnO₂ cathodes with a 2 M ZnSO₄ electrolyte containing 0.2 M MnSO₄.

RESULTS AND DISCUSSION

Self-Recovery Chemistry in MnO₂ Electrodes of Zn-Ion Batteries

Figure 1A presents the galvanostatic cycling stability of aqueous Zn-ion batteries working with several different MnO₂-based cathodes. Here, the capacity was calculated based on the mass of the initial weight of solid MnO₂ on the cathode. For fair comparison, parameters including (1) the mass loading of cathode (area: 0.5 cm², areal loading of MnO₂: ~2.0 mg cm⁻²), (2) the concentration of MnSO₄ additive (0.2 M), and (3) the volume of electrolyte (200 μL for each battery) were well-controlled for all batteries. The δ-MnO₂ cathode synthesized via a molten-salt-assisted method (see Transparent Methods) showed an initial discharge capacity of 252 mAh g⁻¹, and reached 317 mAh g⁻¹ after a five-cycle activation process (Figure 1A). Unlike most of the previously reported works, it is interesting that the discharge capacity of the δ-MnO₂ cathode kept increasing during subsequent cycling at a current density of 300 mA g⁻¹, and reached a discharge capacity of 403 mAh g⁻¹ after 100 cycles. α-MnO₂, another cathode material widely utilized in Zn-ion batteries, was also evaluated for its cycling stability. Although showing better discharge capacities in the first five cycles (first discharge: 325 mAh g⁻¹ and fifth discharge: 339 mAh g⁻¹), the α-MnO₂ cathode exhibited inferior capacity retention to that of the δ-MnO₂ cathode. It suggests that different cathodes delivered different electrochemical behaviors in Zn-ion batteries.

The different capacity variation tendencies of these two cathodes point to a fact that is seldom noticed: The capacity of Zn-ion battery cathodes may not be simply determined, as previously reported, by the capability of suppressing Mn-based cathode dissolution. The intrinsic property of the cathode (e.g., the specific surface area, the valent state of Mn cations, and Mn-site defects) may result in the change of parameters that were not given sufficient attention, i.e., the oxidation of the Mn^{2+} ion in the electrolyte that can lead to the deposition of active Mn compound on the cathode. Considering the abundant defects in the δ-MnO_2 cathode material as synthesized under an unstable, highly oxidizing atmosphere generated by the molten sodium nitrate salt (Hu et al., 2017), modification of δ-MnO_2 was conducted using a facile method where the oxide was stirred in 1 M $CoCl_2$ at room temperature (see Transparent Methods). Compared with the original δ-MnO_2, the resulting cobalt-modified δ-MnO_2 showed an even more pronounced capacity enhancement (Figure 1A), increasing from the initial discharge capacity of 196 mAh g^{-1} to 258 mAh g^{-1} after five cycles and further to 435 mAh g^{-1} at the 100th discharge. This capacity is surprisingly high when compared with the previously reported values ($\sim$300 mAh g^{-1} in the 100th discharge) (Pan et al., 2016; Huang et al., 2018; Zhang et al., 2017).

The increment of the capacity could be highly associated with the oxidation of Mn^{2+} in the electrolyte, which was evidenced by the analysis of Coulumbic efficiency and the differential capacity (dQ/dV). All the cathodes showed high Coulumbic efficiency close to 100%, whereas the cobalt-modified δ-MnO_2 showed slightly lower Coulumbic efficiencies during the recharging cycles (Figure 1B). Without the $MnSO_4$ additive, the Coulumbic efficiency of all samples is similar and near 100% (Figures 1B, capacity data shown in S1). This indicates that the additional Mn^{2+} in the electrolyte was actually involved in the redox process on the cathode. To further investigate this issue, the first five discharge-charge profiles of the cobalt-modified δ-MnO_2 cathode are presented in Figure 1C. Two conventional plateaus at potentials of 1.4 and 1.3 V versus Zn/Zn^{2+} reflect the H^+ intercalation process and the Zn^{2+} intercalation process, respectively (Huang et al., 2018). In each subsequent charging process, an additional plateau/slope was observed at potential around 1.6–1.8 V, besides the two conventional plateaus that represent the reverse process of Zn^{2+} and H^+ intercalation. In Figure 1D, differential capacity (dQ/dV) analysis more clearly shows this additional oxidation process happening at a voltage range of 1.62–1.80 V. This could be ascribed to the oxidation of Mn^{2+} to Mn^{3+}, as will be discussed in the following sections. In a mild aqueous electrolyte environment, subsequent hydrolysis of Mn^{3+} could result in the deposition of Mn compound on the cathode (Gibson et al., 2016). These compounds were involved in the subsequent discharge, thus providing additional capacity.

Figure 1E gives a schematic and an equation that describe the dynamic capacity of a Mn-based cathode. Based on the fact that no matter what be the phase structures of the Mn-based cathode (e.g., α-MnO_2, δ-MnO_2), the discharge capacity of the cathode mainly originates from the redox of Mn species between different valent states (from +4 to +3 or even to +2). Therefore, the discharge capacity of a Mn-based cathode on a specific cycle is determined by three essential parameters and their interaction (Figure 1E): (1) the initial amount and valence of Mn in the solid Mn-based cathode before cycling, (2) the dissolution amount of the active Mn compound during each discharge/charge cycle, and (3) the deposition amount of active Mn compound during each charge. In these parameters, the initial valent state of the Mn element is determined by the cathode material itself, which has a significant influence on the first discharge capacity. On the subsequent cycling, the dissolution rate and deposition rate will negatively and positively, respectively, influence the amount of Mn on the cathode, thereby playing a more important role in the capacity retention. Based on this equation, developing a cathode with a low dissolution rate and a high deposition rate is crucial to the stable operation of Zn-ion batteries.

The synthesis of δ-MnO_2 and its further modification by cobalt were illustrated in Figure 2A (details are provided in the Supplemental Information) (Hu et al., 2017). As indicated by the qualitative analysis of the Mn L-edge near-edge X-ray absorption fine-structure (NEXAFS) spectra (Cowie et al., 2010; Gann et al., 2016) (Figure 2D), cobalt-modified δ-MnO_2 showed the lowest Mn valency among the three different MnO_2-based cathodes. Therefore an expected lower initial capacity was observed for cobalt-modified δ-MnO_2. For the batteries without any additional $MnSO_4$ in the electrolyte, the dissolution rate is reflective of the capacity retention. As shown in Figure 1B, the dissolution rate of cobalt-modified δ-MnO_2 is only slightly lower than those of the other two cathodes. Based on these results, the significant capacity increment of cobalt-modified δ-MnO_2 during cycling could be attributed to its superior deposition rate of Mn compound. A comparison of the dQ/dV profile of the fifth charging (Figure 1F) also indicates that the additional oxidation process on a δ-MnO_2 cathode with cobalt modification is more significant than that without cobalt modification. Furthermore, the cobalt-modified δ-MnO_2 cathode shows excellent rate performance
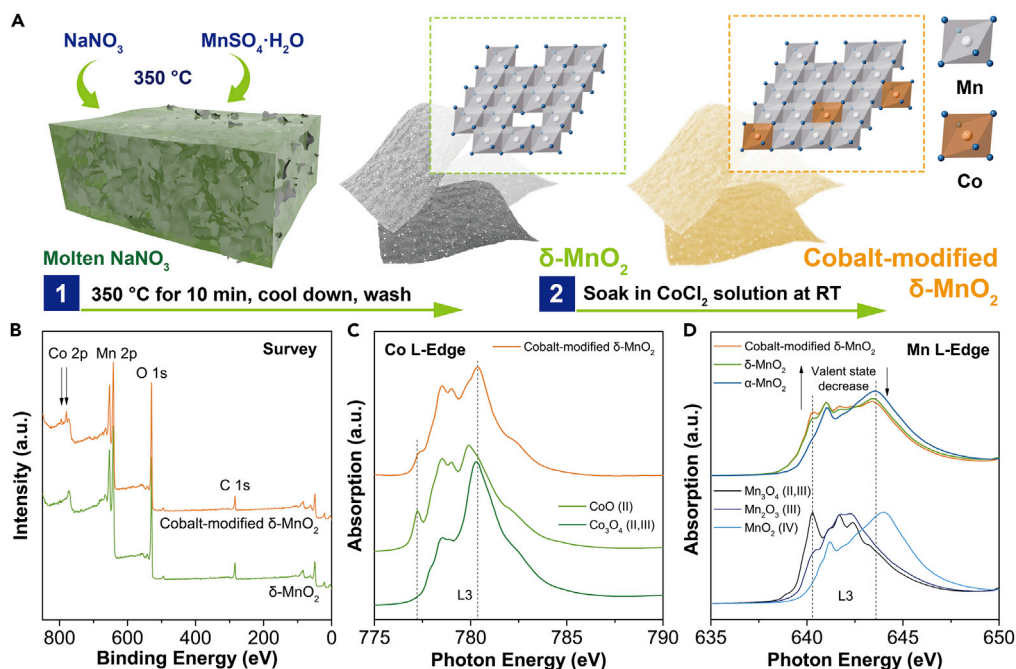
Figure 2. Synthesis and Characterization of Cobalt-Modified δ-MnO$_2$

(A) Illustration of the synthesis procedure of cobalt-modified δ-MnO$_2$, and schematic demonstration of incorporating positions of the Co species on the layered δ-MnO$_2$.

(B) XPS survey profiles of δ-MnO$_2$ and cobalt-modified δ-MnO$_2$.

(C) Co L-edge NEXAFS spectra (TEY mode) of cobalt-modified δ-MnO$_2$.

(D) Mn L-edge NEXAFS spectra (TEY mode) of the three MnO$_2$ materials.

and rate retention (over 500 mAh g^{-1} at 0.1 mA g^{-1} and ~125 mAh g^{-1} at 5 mA g^{-1}) after 100 cycles of cathode recovery (Figure 1G). In the following sections, we analyze the property of the material and design a first-reported home-made electrolyzer system to offer more insights into the role of the cobalt-containing species on the mechanism behind the unique performance.

The existence of the cobalt element and its chemical state is crucial to the deposition rate of the cobalt-modified δ-MnO$_2$ cathode material. The presence of the Co was revealed by Co 2p peaks (2p$_{3/2}$ at 795.5 eV and 2p$_{1/2}$ at 780.7 eV) in the spectra of X-ray photoelectron spectroscopy (XPS) (Figures 2B and S2). The quantity of cobalt element was further evaluated with inductively coupled plasma-optical emission spectrometry (ICP-OES), which gave a Co/Mn atomic ratio of 0.063:1 after cobalt modification (Table S1). A similar result of Co/Mn ratio (0.052:1) was also obtained by the compositional analysis of the XPS survey spectra (Table S2). These results from both bulk-sensitive ICP and surface-sensitive XPS indicate that Co element is evenly decorated on the δ-MnO$_2$. Evidence from the Co L-edge NEXAFS spectra (Figure 2C) suggests that Co species on the cobalt-modified δ-MnO$_2$ has a valent state between +2 and +3. This indicates that during the modification process, Co^{2+} in the CoCl$_2$ solution was partially oxidized by the high-valent-state (+4) Mn cations in the δ-MnO$_2$. Meanwhile, the valent state of Mn cation was decreased, as evidenced by the Mn L-edge NEXAFS spectra (Figure 2D). Owing to the presence of Mn-site defects, cobalt-containing species (e.g., Co(II) and Co(III)) can be incorporated in δ-MnO$_2$ nanosheets (as illustrated in Figure 2A). (Wang et al., 2018) In addition, X-ray diffraction (XRD, Figure S3) and selected area electron diffraction (SAED, Figure 3C) patterns of the material show no other well-defined crystalline phase. Detailed observation of the transmission electron microscopic (TEM) and high-resolution TEM (HR-TEM) images did not reveal the existence of any amorphous phase other than the layer-structured manganese oxide. Energy-dispersive X-ray (EDX) mapping in Figure 3F indicates that cobalt element is well dispersed on the cobalt-modified δ-MnO$_2$ with no significant agglomeration. In short, after cobalt modification, cobalt cations with valent states +2 and +3 in the form of cobalt-containing species is incorporated in the highly defective δ-MnO$_2$ nanosheets. A similar conclusion was also drawn by Wang et al. based on analysis of the quick extended X-ray absorption fine structure data (Wang et al., 2018).
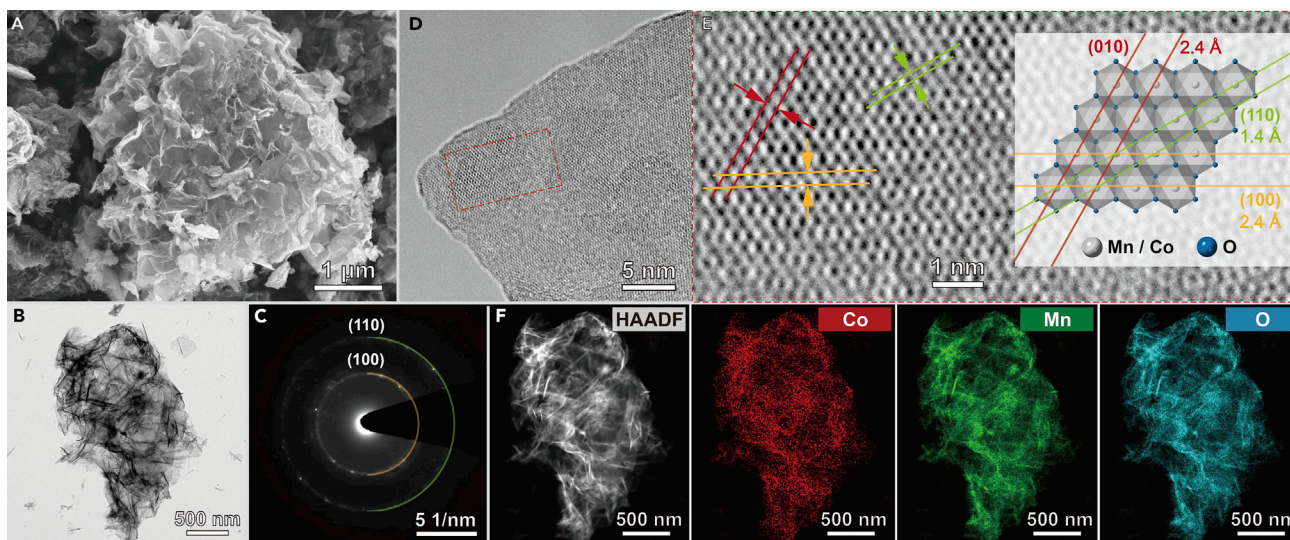
Figure 3. Microscopic Characterization of Cobalt-Modified δ-MnO₂

(A–F) (A) Scanning electron microscopic, (B) TEM, (C) SAED pattern, (D and E) HR-TEM, and (F) EDX mapping of cobalt-modified δ-MnO₂.

Resulting from the removal of the salts after the molten-salt synthesis, the δ-MnO$_2$ nanosheets formed loose-packed particles with a size of several micrometers (Figure S4). The loose packing morphology results in abundant secondary pores, which demonstrates a high specific surface area (139 m^2 g^{-1}) and a large total pore volume (0.50 cm^3 g^{-1}), as presented in Figure S5. Owing to the mild condition utilized for the cobalt modification, the resulting material shows a flower-like morphology (Figure 3A), exhibiting similar surface area (161 m^2 g^{-1}) and porosity (0.48 cm^3 g^{-1}) (Figure S5). Based on the observation of TEM images, the thickness of the cobalt-modified δ-MnO$_2$ nanosheets is approximately 5 nm (Figures 3B and S6). This value was in accordance with the linear analysis of the 2D height sensor signals using atomic force microscopy (Figure S7), which indicates that the thickness is in the range 3–5 nm. HR-TEM in Figures 3D and 3E demonstrates the [001] view direction of the cobalt-modified δ-MnO$_2$ nanosheet, which clearly shows the (010), (100), and (110) planes with a lattice distance of 2.4, 2.4, and 1.4 Å, respectively. This result is also confirmed by the SAED (Figure 3C) and XRD (Figure S3) patterns.

The Catalytic Effect of Cobalt Components in the Deposition Process of Active Mn Compound

In this section, the role of cobalt components in the deposition of active Mn compound is further discussed using cyclic voltammetry (CV) and linear sweep voltammetry (LSV) for a practical battery configuration and a home-made electrolyzer cell. Compared with the galvanostatic charging process where the time duration in the range of 1.6–1.8 V for each charging is very short (causing a fast voltage buildup due to the full charge of the cathode), the CV and LSV methods allow equal time at every voltage step. Therefore, well-defined peaks could be identified from a CV or an LSV curve, when compared with the dQ/dV profile extracted from a galvanostatic charging profile.

Using a conventional Zn|electrolyte|MnO$_2$ coin-type battery configuration, an oxidation peak at around 1.65 V was observed, indicative of the oxidation of Mn^{2+}. It is no surprise that without introducing MnSO$_4$ into the electrolyte, the oxidation of Mn^{2+} is much less significant (Figure S8). Also, in the same electrolyte composition, the oxidation peaks at 1.65 V of the cobalt-modified δ-MnO$_2$ cathode were more noticeable than those of the δ-MnO$_2$ cathode, as presented in Figure 4A.

To further reveal the role of cobalt components, a home-made electrolyzer cell with a two-electrode configuration was designed (Figure S9A). A stainless-steel (SS) electrode or a Co(OH)$_2$-coated SS electrode (denoted as SS-Co(OH)$_2$, preparation setup shown in Figure S10) was used as the working electrode. A Zn plate was used as both the reference and the counter electrode. A larger quantity (10 mL) of the electrolyte with the same composition (2 M ZnSO$_4$ + 0.2 M MnSO$_4$) was used. An LSV scan from 1.0 to 2.3 V (oxidizing process) was applied to the SS electrode and SS-Co(OH)$_2$ electrode.
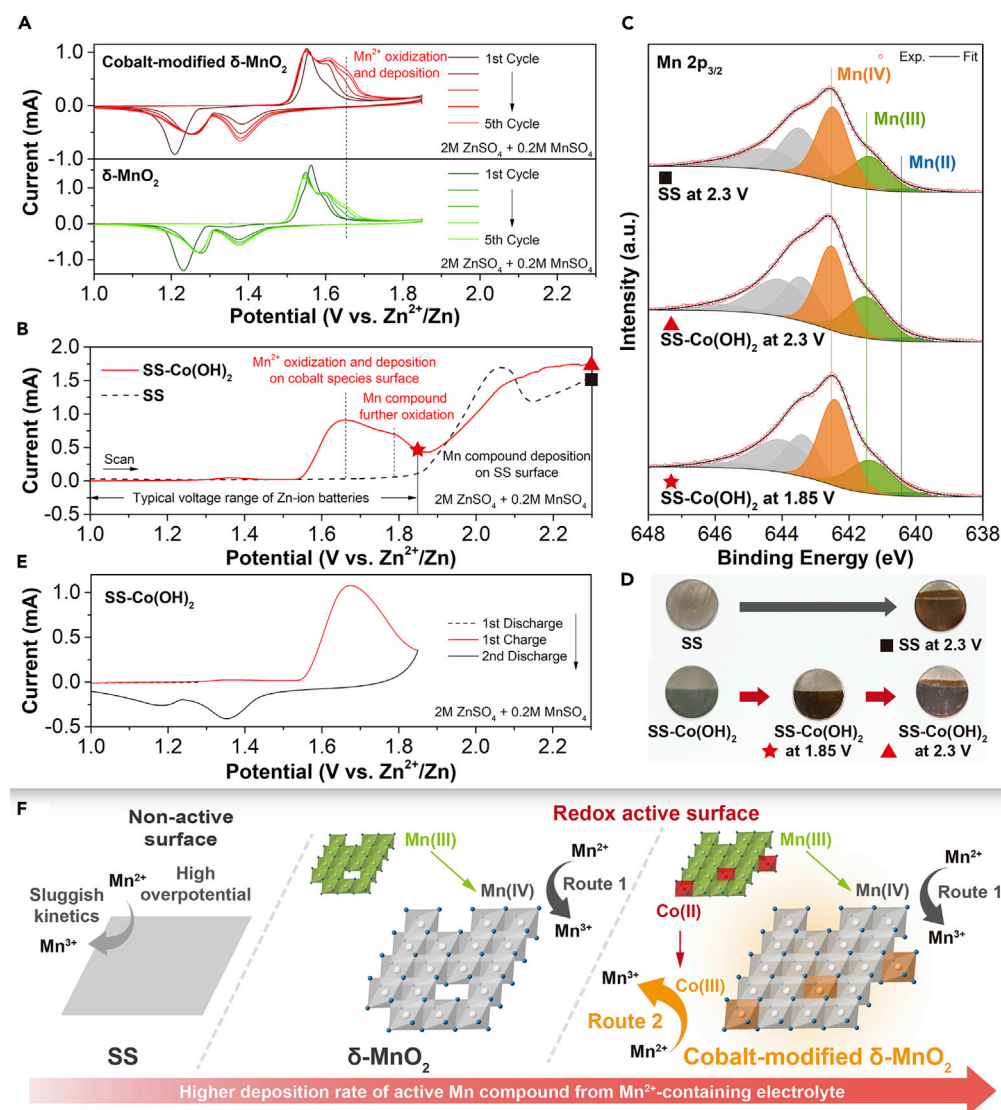
Figure 4. Catalytic Effect of Cobalt Components in the Deposition Process of Active Mn Compound

(A) Comparison of CVs (0.1 mV s^{-1}) of coin-type batteries using δ-MnO$_2$ cathodes with or without cobalt modification.

(B) Comparison of LSV profiles (positive sweep, 1 mV s^{-1}) of stainless steel (SS) and SS covered with pre-electrodeposited Co(OH)$_2$.

(C and D) (C) Mn 2p$_{3/2}$ XPS profiles and (D) digital photographs of the samples after the LSV positive sweep to specific potentials.

(E) First two CV cycles (1 mV s^{-1}) of SS with pre-electrodeposited Co(OH)$_2$.

(F) Illustration of mechanism of the catalysis effect via Mn self-catalysis (Route 1) and via cobalt-induced catalysis (Route 2). Note that results in (B–E) are obtained based on a home-made electrochemical cell (See Figure S9A).

For SS electrode, with the onset voltage at ∼1.85 V, an oxidation peak centered at ∼2.05 V was observed (Figure 4B). Without any Mn compound on the original electrode, this process can be attributed to the oxidation of the Mn^{2+} in the electrolyte. After scanning to 2.3 V, the electrode (denoted as ■ in Figures 4B–4D) was collected and characterized with XPS. The Mn 2p$_{3/2}$ profile of the sample indicates that the deposited Mn compound was mainly in high valent states of +3 and +4 (Figure 4C). For the SS-Co(OH)$_2$ electrode, two additional peaks centered at ∼1.65 V and ∼1.80 V were identified, which could be ascribed to the oxidation of Mn^{2+} in the electrolyte and the further oxidation of Mn compound (e.g., from +3 to +4) on the solid electrode (Figure 4B). The Mn 2p$_{3/2}$ profile (Figure 4C) of the SS-Co(OH)$_2$ electrode after scanning to 1.85 V (denoted as ★) shows that the chemical state of the deposited Mn compound was very similar to those of SS and SS-Co(OH)$_2$ after scanning

to 2.3 V (denoted as ■ and ▲). XRD profiles of the SS-Co(OH)$_2$ after scanning to 1.85 and 2.3 V (denoted as ★ and ▲) indicate that their phase strutures are similar to those of the layered δ-MnO$_2$ and cobalt-modified δ-MnO$_2$ (Figure S11). As presented in the digital photographs (Figure 4D), the major color and texture changes of the SS electrode and SS-Co(OH)$_2$ electrode before and after the LSV scan to a certain voltage also provide visual support for the deposition of the Mn compound.

The high valent state of the Mn compound of the SS-Co(OH)$_2$ sample after scanning to 1.85 V (★) indicates the readiness to be reduced and to provide capacity in a subsequent discharge process. In Figure 4E, the SS-Co(OH)$_2$ electrode was CV scanned (1 mV s^{-1}). No reduction peak was found at the first negative scan from open circuit voltage (~1.28 V) to 1.0 V, indicating that no significant discharging capacity was provided from SS-Co(OH)$_2$. The following positive (oxidation) scan from 1.0 to 1.85 V shows the oxidation of Mn^{2+} and further oxidation as mentioned earlier, after which the subsequent negative scan shows two well-defined peaks at ~1.4 and ~1.2 V (Figure 4E), matching well with the reduction peaks observed from the cobalt-modified δ-MnO$_2$ cathode in a typical Zn-ion battery (Figure 4A).

It is important to note that cobalt element in the state of unbound Co^{2+} in the electrolyte did not facilitate the deposition of active Mn compound. As presented in Figure S12, LSV of SS in the electrolyte with and without additional 0.01 M CoSO$_4$ demonstrated similar onset potentials of ~1.9 V, indicating no beneficial effect on facilitating the Mn compound deposition. Therefore, the promoted deposition of active Mn compound would be ascribed to the cobalt hydroxides and cobalt-containing species that bound on the solid cathode. This result is vital for the analysis in the following section.

The mechanism behind the facilitated deposition of active Mn compound could be ascribed to dual-catalysis effects from Mn(IV) species and Co(III) species on the cathode. Usually, Mn^{2+} in the electrolyte is more stable than most of the Mn cations due to the high tendency of Mn^{3+} disproportionation (Gibson et al., 2016). A recent research reported by Qiao's group indicated that the deposition of MnO$_2$ on a carbon fiber using a Mn^{2+}-containing electrolyte took place at a high potential of 2.2 V versus Zn^{2+}/Zn in a chronoamperometry charge process (Chao et al., 2019). The sluggish kinetics of the direct oxidation of Mn^{2+} could result in a large overpotential. Our LSV scan for the SS electrode in the Mn^{2+}-containing electrolyte (Figure 4B) also indicates a similar result where an onset potential of deposition of the active Mn compound was higher than 1.85 V versus Zn^{2+}/Zn, which is beyond the voltage window for a typical Zn-ion battery. The unique facilitated deposition observed in this work within the voltage range below 1.85 V could be ascribed to the following two different catalysis routes (Figure 4F):

Mn self-catalysis (Route 1): where oxidation of Mn^{2+} was achieved by the comproportionation of Mn(IV) and Mn^{2+}

$$\text{Mn(III)} \rightarrow \text{Mn(IV)} + \text{e}^-$$

$$\text{Mn(IV)} + \text{Mn}^{2+} \rightarrow \text{Mn(III)} + \text{Mn}^{3+}$$
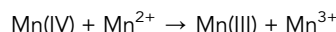
Co-induced catalysis (Route 2): where oxidation of Mn^{2+} was enhanced by cobalt-facilitated charge transfer

$$\text{Co(II)} \rightarrow \text{Co(III)} + \text{e}^-$$

$$\text{Co(III)} + \text{Mn}^{2+} \rightarrow \text{Co(II)} + \text{Mn}^{3+}$$
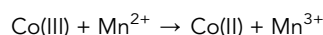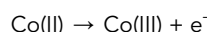
After the oxidation process, the generated Mn^{3+} is then hydrolyzed and deposited as solid Mn(III) compounds on the cathode (Gibson et al., 2016).

For cobalt-modified δ-MnO$_2$ cathode, both catalysis routes contribute to the deposition process. Of importance, the well-dispersed cobalt-containing species could serve as preferred active sites by providing enhanced charge-transfer capability, thereby demonstrating a much superior deposition rate. On the contrary, the deposition of active Mn compound was still observed but less significant (Figure 4A) for the cathode without cobalt modification, as the catalysis could only rely on the Mn self-catalysis route.
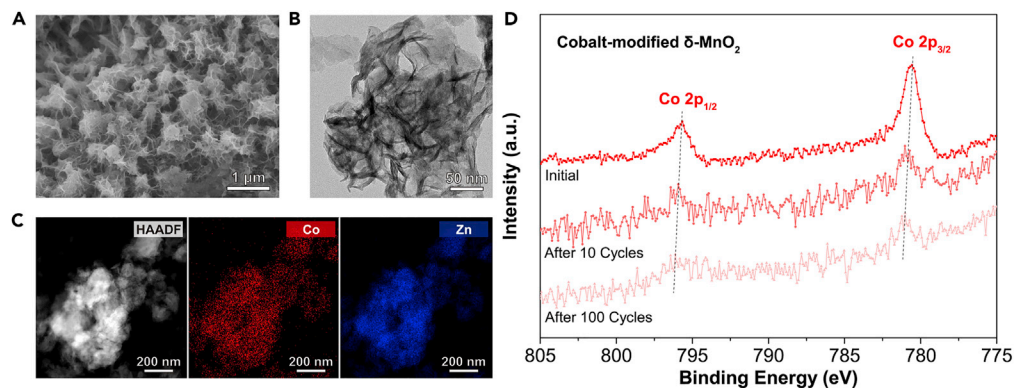
Figure 5. Investigation of the Cobalt Component Before and After Cycling

(A–C) (A) Scanning electron microscopic, (B) TEM, and (C) EDX mapping images of cobalt-modified δ-MnO$_2$ cathode after 100 cycles.

(D) Co 2p XPS profiles of cobalt-modified δ-MnO$_2$ cathode at open circuit voltage before cycling and charged state after 10 and 100 cycles.

It is worth noting that the cobalt content can influence the deposition of Mn compound. Manganese oxide cathodes with different cobalt contents were compared in Figure S13. The increase in cobalt content provides a better capability for the deposition of Mn compounds on the cathode, thereby leading to faster increases of capacities (Figure S13B). The improvement of the deposition of Mn compounds is not very significant when the Co/Mn ratio is higher than 0.10:1 (atom %), indicating that the cobalt-induced facilitation of the deposition of Mn compounds may have a limitation. Also, the deposition of Mn compounds may be influenced by the concentration of the Zn^{2+} ion. As presented in Figure S14, batteries with lower Zn^{2+} concentrations demonstrated higher retention rates. This could be associated with the higher ionic conductivities and higher pH values of the electrolytes, which are both beneficial to the deposition of Mn compounds (Zhang et al., 2016; Poyraz et al., 2019).

The Dynamic Movement of Cobalt Components for Self-Recovery of the Mn-Based Cathode

As shown previously in Figure 1A, the cobalt-modified δ-MnO$_2$ cathode exhibits a superior rate toward the deposition of active Mn compound during the entire cycling test. This result indicates the continuous influence of cobalt components on facilitating the recovery of the Mn-based cathode. The authors once considered that the cobalt components could be only confined on the initial δ-MnO$_2$ cathode. In other words, the newly deposited Mn compound (Figures 5A and 5B) on the surface might not contain cobalt components. Interestingly, however, after 10 and 100 cycles, identical cobalt signals were still observed both in bulk-sensitive EDX spectra (Figures 5C and S15) and in surface-sensitive Co 2p XPS profiles (Figure 5D), although both signals were decreased as expected. This could be attributed to a dynamic movement of cobalt components, similar to the dissolution-deposition process of the MnO$_2$ cathode.

It is important to note that the pH value of the electrolyte could be one of the important parameters that may cause the dissolution and redeposition of cobalt components. The pH value of the electrolyte (2 M ZnSO$_4$ + 0.2 M MnSO$_4$) is ~5 (Sun et al., 2017), a mild acidic environment under which the cobalt components (e.g., Co(OH)$_2$) could be unstable (Gayer and Garrett, 1950). As indicated in previous reports, the electrolyte pH of Zn-ion batteries may vary due to the intercalation/de-intercalation of H$^+$. In a system with a large volume of electrolyte (e.g., 10 mL, experiment shown in Figure 4E), the intercalation/de-intercalation of H$^+$ is not significant enough to largely influence the pH value. Decomposition of Co(OH)$_2$ was observed only after five CV cycles (1.0–1.85 V, Figure S16). However, in a coin-type battery with a small amount of electrolyte (200 μL in each of our battery), the pH value of the electrolyte could be significantly increased after being fully discharged (Lee et al., 2016). The pH increase after the first discharge to 1.0 V was evidenced by the formation of zinc hydroxide sulfate hydrate (which only forms in high pH environment) on the cathode surface, as confirmed by XRD analysis (Figure S17). (Huang et al., 2018; Pan et al., 2016)

In Figure 6, a bigger picture of the role of cobalt components in facilitating the recovery of the cathode and their dynamic movement is demonstrated. During the cycling, cathode reconstruction occurs in the battery, involving the dissolution and deposition of both Mn and Co components. Deposition of the Mn-based
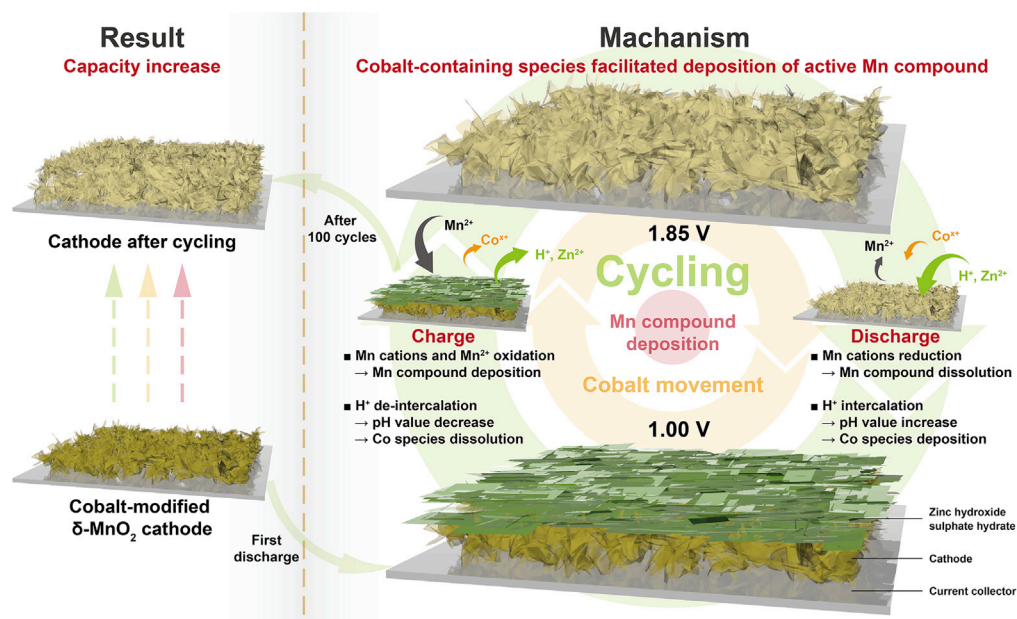
Figure 6. Schematic Illustration of the Whole Picture of This Work: the Dynamic Movement of Cobalt Components during Discharge and Charge of the Batteries and Its Influence on Facilitating Deposition of Active Mn Compound

cathode is driven by an electrochemical charge process, which is further facilitated by cobalt components bound on the Mn compound. At the same time, the deposition/dissolution of the Co component is a pH-sensitive process. Owing to the weak acidic environment, a small fraction of cobalt component was dissolved in the electrolyte. During battery discharging, H^+ was inserted in the Mn-based cathode (Sun et al., 2017), resulting in the increase of pH value and consequently the re-deposition of cobalt component on the reconstructed cathode surface. During each charge process, H^+ was reversibly released, causing the re-dissolution of cobalt components to some extent. This dynamic movement of the cobalt component in the solid electrode and liquid electrolyte is important for the persistent facilitation of cathode recovery.

It is worth mentioning that apart from the facilitating effect from cobalt components, the overall capacity recovery rate of the Mn-based cathode is also limited by many other factors, e.g., (1) limited conductive cathode surface, (2) decreased Mn^{2+} concentration in the electrolyte after many discharging-charging cycles, (3) the ionic conductivity and pH of the electrolyte, and (4) deterioration of the Zn anode (Ha and Lee, 2016; Selvakumaran et al., 2019). From the consideration of the first factor, the increment of the capacity for a battery with the cobalt-modified δ-MnO$_2$ cathode (as shown in Figure 1G) gradually slowed down during the 50–100 cycles. In addition, a comparison of the morphologies of cathode surface before cycling and after 100th charge provides clear evidence that most of the conductive surface (e.g., current collector and conductive carbon) was heavily covered with dense, newly deposited active Mn compound (Figures S18C and S18E). The deterioration of the charge-transfer situation of cathode surface could further limit the deposition of active Mn compound.

Cycling Performance and More Practical Battery Configurations

The practical viability of the cobalt-modified δ-MnO$_2$ cathode was further demonstrated with a prolonged cycling test based on a higher current density of 2 A g^{-1} in a 200 μL electrolyte of 2 M ZnSO$_4$ and 0.2 M MnSO$_4$ (Figure 7A). A commercially applicable battery cycle life (80% of capacity retention) of 2,000 discharge-charge cycles is presented. Even after 5,000 cycles, the battery still shows decent capacity retention of approximately 63% (compared with the 10th discharge capacity). As mentioned in the Introduction section, as the Mn^{2+} additive is also active during cycling, it should also be considered for the evaluation of the overall capacity of the cathode. From the practical utility aspect, the final objective is to stabilize the battery performance with minimum additional Mn^{2+}. Using a smaller electrolyte volume of 70 μL, we then investigate the capacity retention of batteries in 2 M ZnSO$_4$ with five different concentrations of
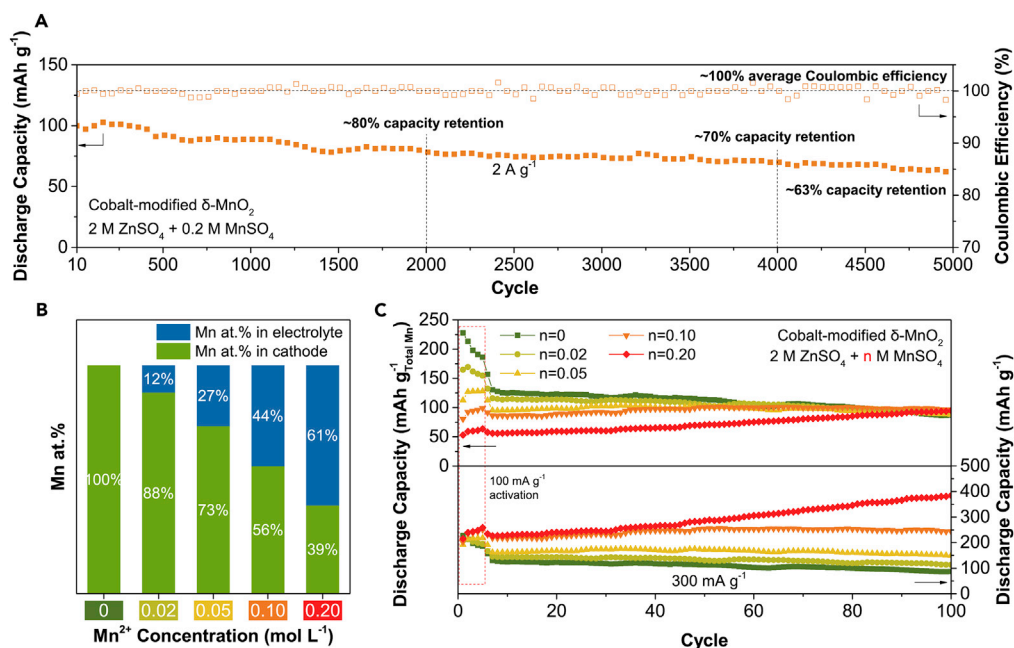
Figure 7. Investigation of Long Cycling Performance and the Electrolyte Compositions

(A) Cycle life and corresponding Coulombic efficiency over 5,000 cycles at 2 A g^{-1} of the batteries with cobalt-modified δ-MnO$_2$ cathode and 200 μL electrolyte.

(B) Comparison of atomic contents of Mn element in electrolyte and cathode.

(C) Comparison of cycling performance for the batteries with 70 μL of aqueous electrolyte containing 2 M ZnSO$_4$ and MnSO$_4$ additives at different concentrations.

MnSO$_4$ additives (from 0 to 0.2 M as demonstrated in Figure 7B) based on the total Mn compound mass (i.e., MnO$_2$ in the solid cathode and MnSO$_4$·H$_2$O added in the electrolyte). As indicated in Figure 7C, due to its good cathode recovery capability, the cobalt-modified δ-MnO$_2$ cathode enabled a more stable operation of rechargeable aqueous Zn-ion batteries. With a low MnSO$_4$ additive concentration of only 0.02 M (corresponding to an atomic percentage of 12% of the Mn additive in the electrolyte), an average capacity fading rate of 0.23% per cycle was achieved between the 7th and 100th cycles, much lower than that without MnSO$_4$ additive (0.35% per cycle, 1.5 times faster fading). We further demonstrate that batteries with a gel-polymer electrolyte and a cobalt-modified δ-MnO$_2$ cathode also presented decent performance and a similar trend of capacity increase during a 100-cycle stability test (Figure S19). This indicates that the cobalt-catalyzed deposition strategy can also be applied to a hydrogel electrolyte battery system.

Conclusion

Stable performance of Zn-ion batteries was realized through a first reported cobalt-catalyzed recovery strategy, which was achieved by facilitating the deposition of active Mn compound in the cathode. The discharge capacity of a Mn-based cathode was determined by (1) the initial amount and valence of Mn in the solid Mn-based cathode before cycling, (2) the dissolution amount of the Mn cathode, and (3) most importantly, the deposition amount of active Mn compound. The facilitation of deposition is achieved by utilizing a facile cobalt modification strategy that integrated the well-dispersed, cobalt-containing species into the defective δ-MnO$_2$ nanosheets. Verified by both practical coin-type batteries and a newly designed home-made electrolyzer system, the deposition of active Mn compound was confirmed to be significantly facilitated with cobalt-based compounds (e.g., Co(OH)$_2$) and the bound cobalt-containing species (e.g., Co(II) and Co(III)) in the cobalt-modified δ-MnO$_2$ cathode, whereas the unbound Co^{2+} in the electrolyte showed no significant impact on the deposition process. In addition, the concentration of Mn^{2+} additives and the volume of the electrolyte are also vital parameters for capacity recovery of the cathode. For a fair performance comparison, these two parameters should be well controlled and clearly indicated in future publications of Mn-based cathode for Zn-ion batteries. Overall, this work provides a deeper insight into the deposition behaviors of the active cathode material and its significant influence on the stable performance of aqueous Zn-ion batteries. This work could also provide inspiration for the materials engineering for future functionalized cathodes, especially for other conversion-type battery

cathodes that suffer from the similar dissolution issue, for example, manganese-based cathodes for Li-ion and Na-ion batteries and sulfur cathodes for Li-S and Na-S batteries.

Limitations of the Study

Our work has demonstrated how cobalt modification can facilitate the deposition of Mn compounds on the δ-MnO_2 cathode and lead to stable performance of Zn-ion batteries. Although the catalytic effect of cobalt species was evidenced by electrochemical analysis and supported by multiple *ex situ* characterizations, in-depth understanding of the catalytic mechanism is still needed. Further investigation with advanced *in situ* techniques and theoretical calculations may provide a deeper insight.

METHODS

All methods can be found in the accompanying Transparent Methods supplemental file.

SUPPLEMENTAL INFORMATION

Supplemental Information can be found online at https://doi.org/10.1016/j.isci.2020.100943.

AUTHOR CONTRIBUTIONS

Z.S. and Y.Z. conceived and designed the research. Y.Z. conducted material synthesis, characterizations, and electrochemical analysis of the batteries and the electrolyzer. Y.Z., X.X., and J.-P.V. conducted the NEXAFS characterization and analysis. Y.Z., X.X., and Z.S. co-wrote the manuscript.

DECLARATION OF INTERESTS

The authors declare no competing interests.

REFERENCES

Alfaruqi, M.H., Mathew, V., Gim, J., Kim, S., Song, J., Baboo, J.P., Choi, S.H., and Kim, J. (2015). Electrochemically induced structural transformation in a γ-MnO_2 cathode of a high capacity zinc-ion battery system. Chem. Mater. *27*, 3609–3620.

Chae, M.S., Heo, J.W., Lim, S.-C., and Hong, S.-T. (2016). Electrochemical zinc-ion intercalation properties and crystal structures of $ZnMo_6S_8$ and $Zn_2Mo_6S_8$ chevrel phases in aqueous electrolytes. Inorg. Chem. *55*, 3294–3301.

Chao, D., Zhou, W., Ye, C., Zhang, Q., Chen, Y., Gu, L., Davey, K., and Qiao, S.-Z. (2019). An electrolytic Zn–MnO_2 battery for high-voltage and scalable energy storage. Angew. Chem. Int. Ed. *58*, 7823–7828.

Cheng, F., Chen, J., Gou, X., and Shen, P. (2005). High-power alkaline Zn–MnO_2 batteries using γ-MnO_2 nanowires/nanotubes and electrolytic zinc powder. Adv. Mater. *17*, 2753–2756.

Cowie, B.C.C., Tadich, A., and Thomsen, L. (2010). The current performance of the wide range (90–2500 eV) soft X-ray beamline at the Australian Synchrotron. AIP Conf. Proc. *1234*, 307–310.

Du, M., Liao, K., Lu, Q., and Shao, Z. (2019). Recent advances in the interface engineering of solid-state Li-ion batteries with artificial buffer layers: challenges, materials, construction, and characterization. Energy Environ. Sci. *12*, 1780–1804.

Fang, G., Zhou, J., Pan, A., and Liang, S. (2018). Recent advances in aqueous zinc-ion batteries. ACS Energy Lett. *3*, 2480–2501.

Fang, G., Zhu, C., Chen, M., Zhou, J., Tang, B., Cao, X., Zheng, X., Pan, A., and Liang, S. (2019). Suppressing manganese dissolution in potassium manganate with rich oxygen defects engaged high-energy-density and durable aqueous zinc-ion battery. Adv. Funct. Mater. *29*, 1808375.

Fu, Y., Wei, Q., Zhang, G., Wang, X., Zhang, J., Hu, Y., Wang, D., Zuin, L., Zhou, T., Wu, Y., et al. (2018). High-performance reversible aqueous Zn-ion battery based on porous MnO_x nanorods coated by MOF-derived N-doped carbon. Adv. Energy Mater. *8*, 1801445.

Gann, E., McNeill, C.R., Tadich, A., Cowie, B.C.C., and Thomsen, L. (2016). Quick AS NEXAFS Tool (QANT): a program for NEXAFS loading and analysis developed at the Australian Synchrotron. J. Synchrotron. Rad. *23*, 374–380.

Gayer, K.H., and Garrett, A.B. (1950). The solubility of cobalt hydroxide, $Co(OH)_2$, in solutions of hydrochloric acid and sodium hydroxide at 25°. J. Am. Chem. Soc. 72, 3921–3923.

Gibson, A.J., Johannessen, B., Beyad, Y., Allen, J., and Donne, S.W. (2016). Dynamic electrodeposition of manganese dioxide: temporal variation in the electrodeposition mechanism. J. Electrochem. Soc. 163, H305–H312.

Ha, S., and Lee, K.T. (2016). Converting to long stability. Nat. Energy 1, 16057.

He, P., Yan, M., Zhang, G., Sun, R., Chen, L., An, Q., and Mai, L. (2017). Layered VS_2 nanosheet-based aqueous Zn ion battery cathode. Adv. Energy Mater. 7, 1601920.

Hu, L., and Xu, K. (2014). Nonflammable electrolyte enhances battery safety. Proc. Natl. Acad. Sci. U S A 111, 3205–3206.

Hu, Z., Xiao, X., Jin, H., Li, T., Chen, M., Liang, Z., Guo, Z., Li, J., Wan, J., Huang, L., et al. (2017). Rapid mass production of two-dimensional metal oxides and hydroxides via the molten salts method. Nat. Commun. 8, 15630.

Huang, J., Guo, Z., Ma, Y., Bin, D., Wang, Y., and Xia, Y. (2019a). Recent progress of rechargeable batteries using mild aqueous electrolytes. Small Methods 3, 1800272.

Huang, J., Wang, Z., Hou, M., Dong, X., Liu, Y., Wang, Y., and Xia, Y. (2018). Polyaniline-intercalated manganese dioxide nanolayers as a high-performance cathode material for an aqueous zinc-ion battery. Nat. Commun. 9, 2906.

Huang, Y., Mou, J., Liu, W., Wang, X., Dong, L., Kang, F., and Xu, C. (2019b). Novel insights into energy storage mechanism of aqueous rechargeable Zn/MnO_2 batteries with participation of Mn^{2+}. Nano-Micro Lett. 11, 49.

Kaveevivitchai, W., and Manthiram, A. (2016). High-capacity zinc-ion storage in an open-tunnel oxide for aqueous and nonaqueous Zn-ion batteries. J. Mater. Chem. A 4, 18737–18741.

Konarov, A., Voronina, N., Jo, J.H., Bakenov, Z., Sun, Y.-K., and Myung, S.-T. (2018). Present and future perspective on electrode materials for rechargeable zinc-ion batteries. ACS Energy Lett. 3, 2620–2640.

Kundu, D., Adams, B.D., Duffort, V., Vajargah, S.H., and Nazar, L.F. (2016). A high-capacity and long-life aqueous rechargeable zinc battery using a metal oxide intercalation cathode. Nat. Energy 1, 16119.

Kundu, D., Vajargah, S.H., Wan, L., Adams, B., Prendergast, D., and Nazar, L.F. (2018). Aqueous vs. nonaqueous Zn-ion batteries: consequences of the desolvation penalty at the interface. Energy Environ. Sci. 11, 881–892.

Lee, B., Seo, H.R., Lee, H.R., Yoon, C.S., Kim, J.H., Chung, K.Y., Cho, B.W., and Oh, S.H. (2016). Critical role of pH evolution of electrolyte in the reaction mechanism for rechargeable zinc batteries. ChemSusChem 9, 2948–2956.

Li, B., Nie, Z., Vijayakumar, M., Li, G., Liu, J., Sprenkle, V., and Wang, W. (2015). Ambipolar zinc-polyiodide electrolyte for a high-energy density aqueous redox flow battery. Nat. Commun. 6, 6303.

Li, H., Ma, L., Han, C., Wang, Z., Liu, Z., Tang, Z., and Zhi, C. (2019a). Advanced rechargeable zinc-based batteries: recent progress and future perspectives. Nano Energy 62, 550–587.

Li, H., McRae, L., Firby, C.J., and Elezzabi, A.Y. (2019b). Rechargeable aqueous electrochromic batteries utilizing Ti-substituted tungsten molybdenum oxide based Zn^{2+} ion intercalation cathodes. Adv. Mater. 31, 1807065.

Li, Y., Wang, S., Salvador, J.R., Wu, J., Liu, B., Yang, W., Yang, J., Zhang, W., Liu, J., and Yang, J. (2019c). Reaction mechanisms for long-life rechargeable Zn/MnO_2 batteries. Chem. Mater. 31, 2036–2047.

Lin, D., Liu, Y., and Cui, Y. (2017). Reviving the lithium metal anode for high-energy batteries. Nat. Nano. 12, 194–206.

Long, J., Gu, J., Yang, Z., Mao, J., Hao, J., Chen, Z., and Guo, Z. (2019). Highly porous, low band-gap $Ni_xMn_{3-x}O_4$ ($0.55 \leq x \leq 1.2$) spinel nanoparticles with in situ coated carbon as advanced cathode materials for zinc-ion batteries. J. Mater. Chem. A 7, 17854–17866.

Lu, Q., Yu, J., Zou, X., Liao, K., Tan, P., Zhou, W., Ni, M., and Shao, Z. (2019). Self-catalyzed growth of Co, N-codoped CNTs on carbon-encased CoS_x surface: a noble-metal-free bifunctional oxygen electrocatalyst for flexible solid Zn–air batteries. Adv. Funct. Mater. 29, 1904481.

Lu, Y., Goodenough, J.B., and Kim, Y. (2011). Aqueous cathode for next-generation alkali-ion batteries. J. Am. Chem. Soc. 133, 5756–5759.

Lukatskaya, M.R., Dunn, B., and Gogotsi, Y. (2016). Multidimensional materials and device architectures for future hybrid energy storage. Nat. Commun. 7, 12647.

Luo, J.-Y., Cui, W.-J., He, P., and Xia, Y.-Y. (2010). Raising the cycling stability of aqueous lithium-ion batteries by eliminating oxygen in the electrolyte. Nat. Chem. 2, 760–765.

Ma, L., Li, N., Long, C., Dong, B., Fang, D., Liu, Z., Zhao, Y., Li, X., Fan, J., Chen, S., et al. (2019). Achieving both high voltage and high capacity in aqueous zinc-ion battery for record high energy density. Adv. Funct. Mater. 29, 1906142.

Ming, J., Guo, J., Xia, C., Wang, W., and Alshareef, H.N. (2019). Zinc-ion batteries: materials, mechanisms, and applications. Mater. Sci. Eng. R. 135, 58–84.

Nam, K.W., Kim, H., Choi, J.H., and Choi, J.W. (2019). Crystal water for high performance layered manganese oxide cathodes in aqueous rechargeable zinc batteries. Energy Environ. Sci. 12, 1999–2009.

Pan, C., Zhang, R., Nuzzo, R.G., and Gewirth, A.A. (2018). $ZnNi_xMn_xCo_{2-2x}O_4$ spinel as a high-voltage and high-capacity cathode material for nonaqueous Zn-ion batteries. Adv. Energy Mater. 8, 1800589.

Pan, H., Shao, Y., Yan, P., Cheng, Y., Han, K.S., Nie, Z., Wang, C., Yang, J., Li, X., Bhattacharya, P., et al. (2016). Reversible aqueous zinc/manganese oxide energy storage from conversion reactions. Nat. Energy 1, 16039.

Poyraz, A.S., Laughlin, J., and Zec, Z. (2019). Improving the cycle life of cryptomelane type manganese dioxides in aqueous rechargeable zinc ion batteries: the effect of electrolyte concentration. Electrochim. Acta 305, 423–432.

Selvakumaran, D., Pan, A., Liang, S., and Cao, G. (2019). A review on recent developments and challenges of cathode materials for rechargeable aqueous Zn-ion batteries. J. Mater. Chem. A 7, 18209–18236.

Song, M., Tan, H., Chao, D., and Fan, H.J. (2018). Recent advances in Zn-ion batteries. Adv. Funct. Mater. 28, 1802564.

Sun, W., Wang, F., Hou, S., Yang, C., Fan, X., Ma, Z., Gao, T., Han, F., Hu, R., Zhu, M., et al. (2017). Zn/MnO_2 battery chemistry with H^+ and Zn^{2+} coinsertion. J. Am. Chem. Soc. 139, 9775–9778.

Verma, V., Kumar, S., Manalastas, W., Jr., Satish, R., and Srinivasan, M. (2019). Progress in rechargeable aqueous zinc- and aluminum-ion battery electrodes: challenges and outlook. Adv. Sustain. Syst. 3, 1800111.

Wan, F., and Niu, Z. (2019). Design strategies for vanadium-based aqueous zinc-ion batteries. Angew. Chem. Int. Ed. 58, 16358–16367.

Wan, F., Zhang, L., Dai, X., Wang, X., Niu, Z., and Chen, J. (2018). Aqueous rechargeable zinc/sodium vanadate batteries with enhanced performance from simultaneous insertion of dual carriers. Nat. Commun. 9, 1656.

Wang, D., Wang, L., Liang, G., Li, H., Liu, Z., Tang, Z., Liang, J., and Zhi, C. (2019a). A superior δ-MnO_2 cathode and a self-healing Zn-δ-MnO_2 battery. ACS Nano 13, 10643–10652.

Wang, J., Wang, J.-G., Liu, H., Wei, C., and Kang, F. (2019b). Zinc stabilized MnO_2 nanospheres for high capacity and long lifespan aqueous zinc-ion batteries. J. Mater. Chem. A 7, 13727–13735.

Wang, Y., Benkaddour, S., Marafatto, F.F., and Peña, J. (2018). Diffusion- and pH-dependent reactivity of layer-type MnO_2: reactions at particle edges versus vacancy sites. Environ. Sci. Technol. 52, 3476–3485.

Wu, B., Zhang, G., Yan, M., Xiong, T., He, P., He, L., Xu, X., and Mai, L. (2018). Graphene scroll-coated α-MnO_2 nanowires as high-performance cathode materials for aqueous Zn-ion battery. Small 14, 1703850.

Xiong, T., Yu, Z.G., Wu, H., Du, Y., Xie, Q., Chen, J., Zhang, Y.-W., Pennycook, S.J., Lee, W.S.V., and Xue, J. (2019). Defect engineering of oxygen-deficient manganese oxide to achieve high-performing aqueous zinc ion battery. Adv. Energy Mater. 9, 1803815.

Xu, C., Li, B., Du, H., and Kang, F. (2012). Energetic zinc ion chemistry: the rechargeable zinc ion battery. Angew. Chem. Int. Ed. 51, 933–935.

Yan, M., He, P., Chen, Y., Wang, S., Wei, Q., Zhao, K., Xu, X., An, Q., Shuang, Y., Shao, Y., et al. (2018). Water-lubricated intercalation in $V_2O_5 \cdot nH_2O$ for high-capacity and high-rate

aqueous rechargeable zinc batteries. Adv. Mater. *30*, 1703725.

Yang, Q., Liang, G., Guo, Y., Liu, Z., Yan, B., Wang, D., Huang, Z., Li, X., Fan, J., and Zhi, C. (2019). Do zinc dendrites exist in neutral zinc batteries: a developed electrohealing strategy to in situ rescue in-service batteries. Adv. Mater. *31*, 1903778.

Yu, P., Zeng, Y., Zhang, H., Yu, M., Tong, Y., and Lu, X. (2019). Flexible Zn-ion batteries: recent progresses and challenges. Small *15*, 1804760.

Zeng, X., Hao, J., Wang, Z., Mao, J., and Guo, Z. (2019). Recent progress and perspectives on aqueous Zn-based rechargeable batteries with

mild aqueous electrolytes. Energy Storage Mater. *20*, 410–437.

Zhang, N., Cheng, F., Liu, J., Wang, L., Long, X., Liu, X., Li, F., and Chen, J. (2017). Rechargeable aqueous zinc-manganese dioxide batteries with high energy and power densities. Nat. Commun. *8*, 405.

Zhang, N., Cheng, F., Liu, Y., Zhao, Q., Lei, K., Chen, C., Liu, X., and Chen, J. (2016). cation-deficient spinel $ZnMn_2O_4$ cathode in $Zn(CF_3SO_3)_2$ electrolyte for rechargeable aqueous Zn-ion battery. J. Am. Chem. Soc. *138*, 12894–12901.

Zhao, B., Ran, R., Liu, M., and Shao, Z. (2015). A comprehensive review of $Li_4Ti_5O_{12}$-based

electrodes for lithium-ion batteries: the latest advancements and future perspectives. Mater. Sci. Eng. R. *98*, 1–71.

Zhong, Y., Xu, X., Wang, W., and Shao, Z. (2019). Recent advances in metal-organic framework derivatives as oxygen catalysts for zinc-air batteries. Batteries Supercaps *2*, 272–289.

Zhu, C., Fang, G., Zhou, J., Guo, J., Wang, Z., Wang, C., Li, J., Tang, Y., and Liang, S. (2018). Binder-free stainless steel@Mn_3O_4 nanoflower composite: a high-activity aqueous zinc-ion battery cathode with high-capacity and long-cycle-life. J. Mater. Chem. A *6*, 9677–9683.

Supplemental Information

Self-Recovery Chemistry and Cobalt-Catalyzed

Electrochemical Deposition of Cathode for

Boosting Performance of Aqueous Zinc-Ion Batteries

Yijun Zhong, Xiaomin Xu, Jean-Pierre Veder, and Zongping Shao
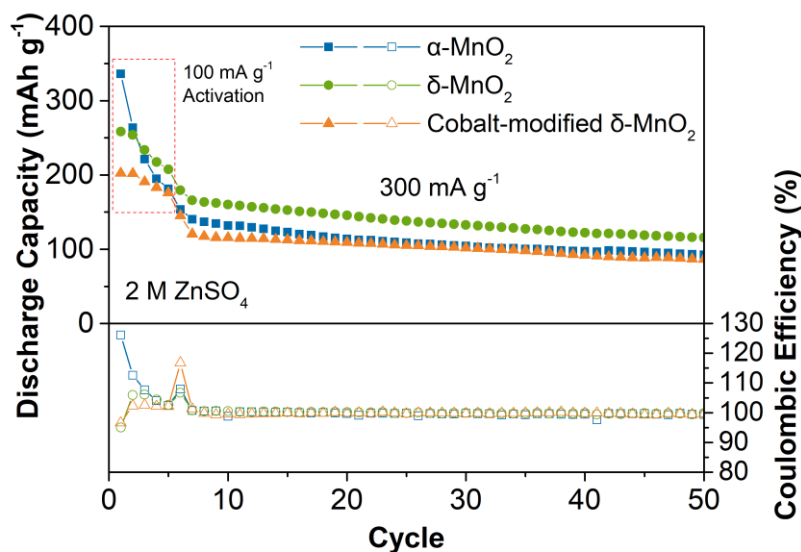
Supplemental Figures and Tables

Figure S1. Comparison of discharge capacities of the manganese oxide cathodes without the additive $MnSO_4$ in the electrolyte at 300 mA g^{-1} for 50 cycles. Related to Figure 1B.
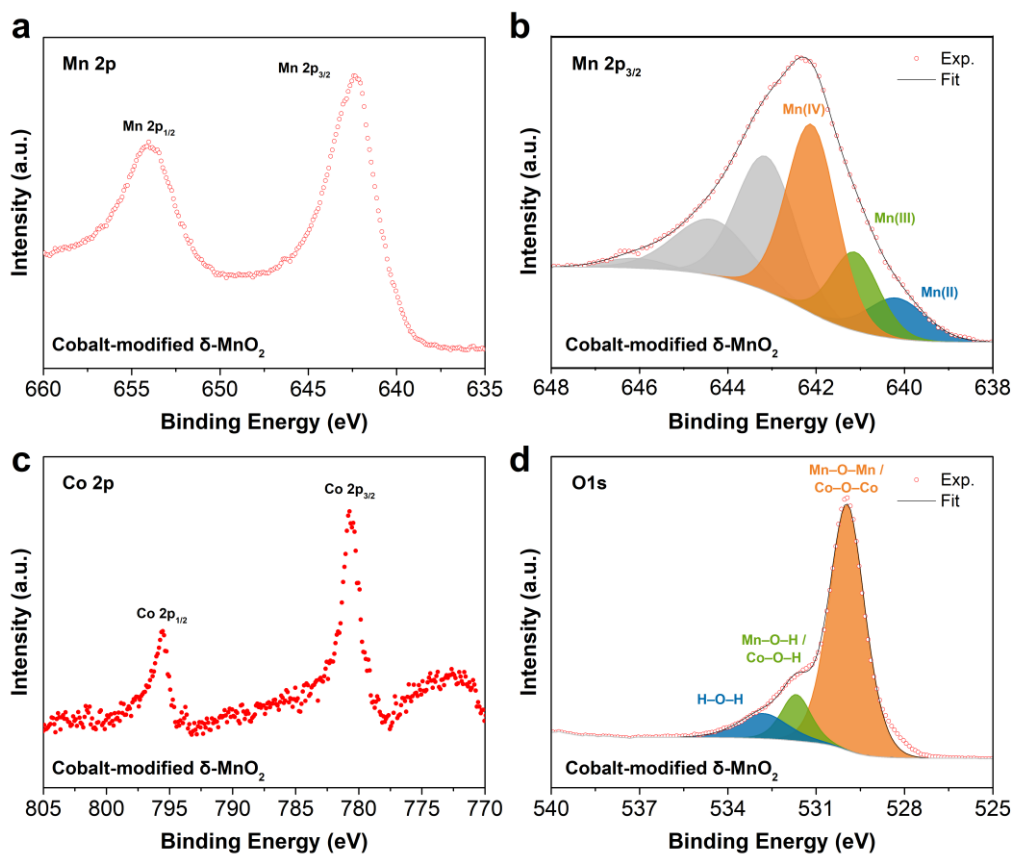

Figure S2. XPS spectra of cobalt-modified δ-MnO_2: a) Mn 2p, b) Mn 2p$_{3/2}$ with peak fitting, c) Co 2p, and d) O 1s with peak fitting. Related to Figure 2B.
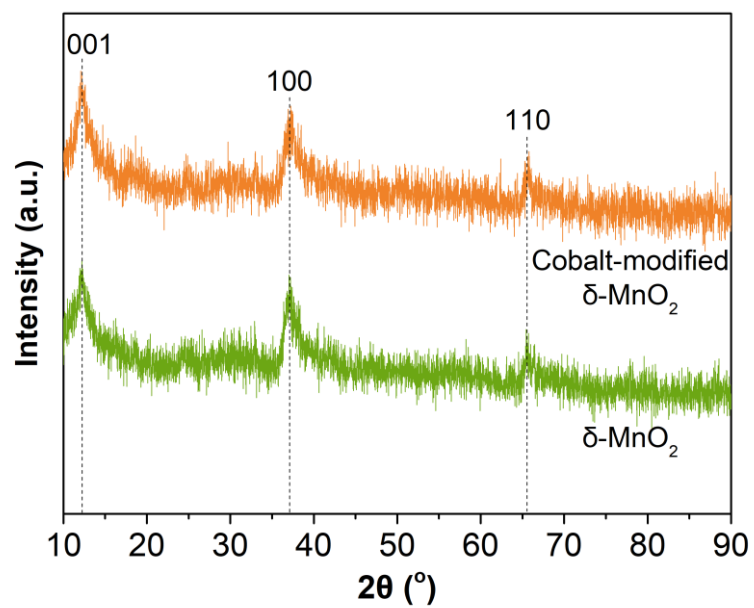
Figure S3. XRD patterns of δ-MnO_2 before and after cobalt-modification. Related to Figure 3.
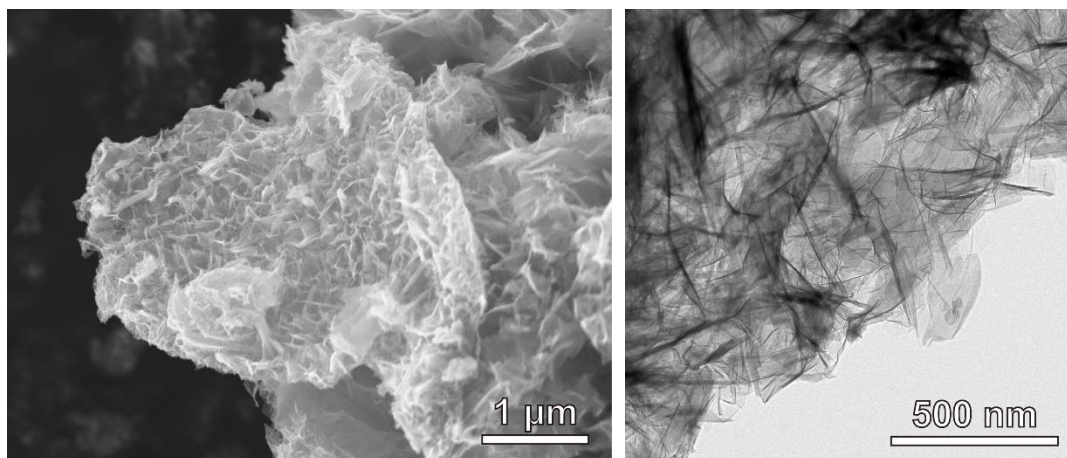
Figure S4. a) SEM and b) TEM images of δ-MnO_2 prepared using a molten-salt method. Related to Figure 3.
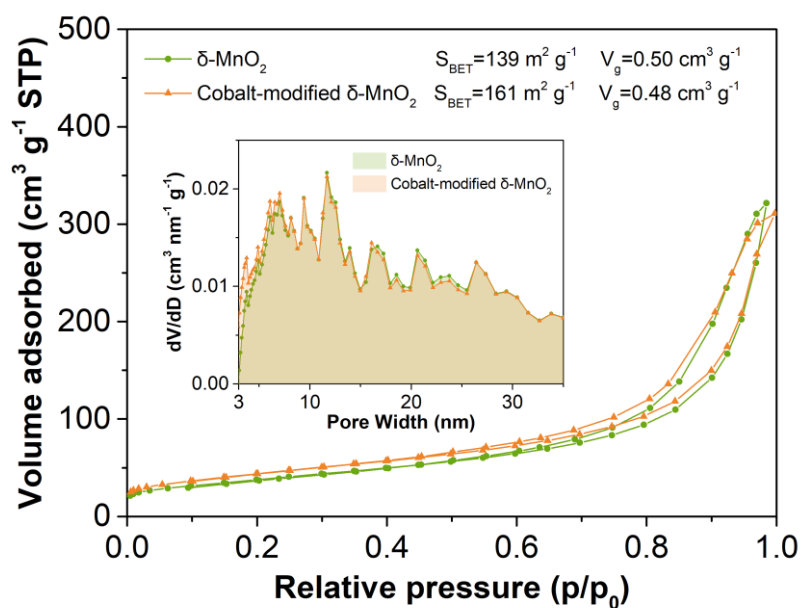
Figure S5. a) N_2 adsorption-desorption isotherms and corresponding pore size distributions of the materials calculated by a QSDFT method. Related to Figure 3.
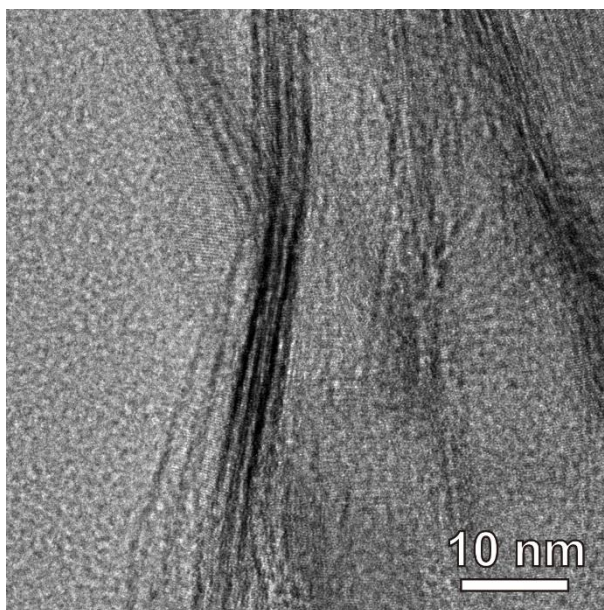
Figure S6. TEM images of cobalt-modified δ-MnO$_2$. The image shows a curved edge of the nanosheet, indicating the thickness of the material is around 5 nm. Related to Figure 3.
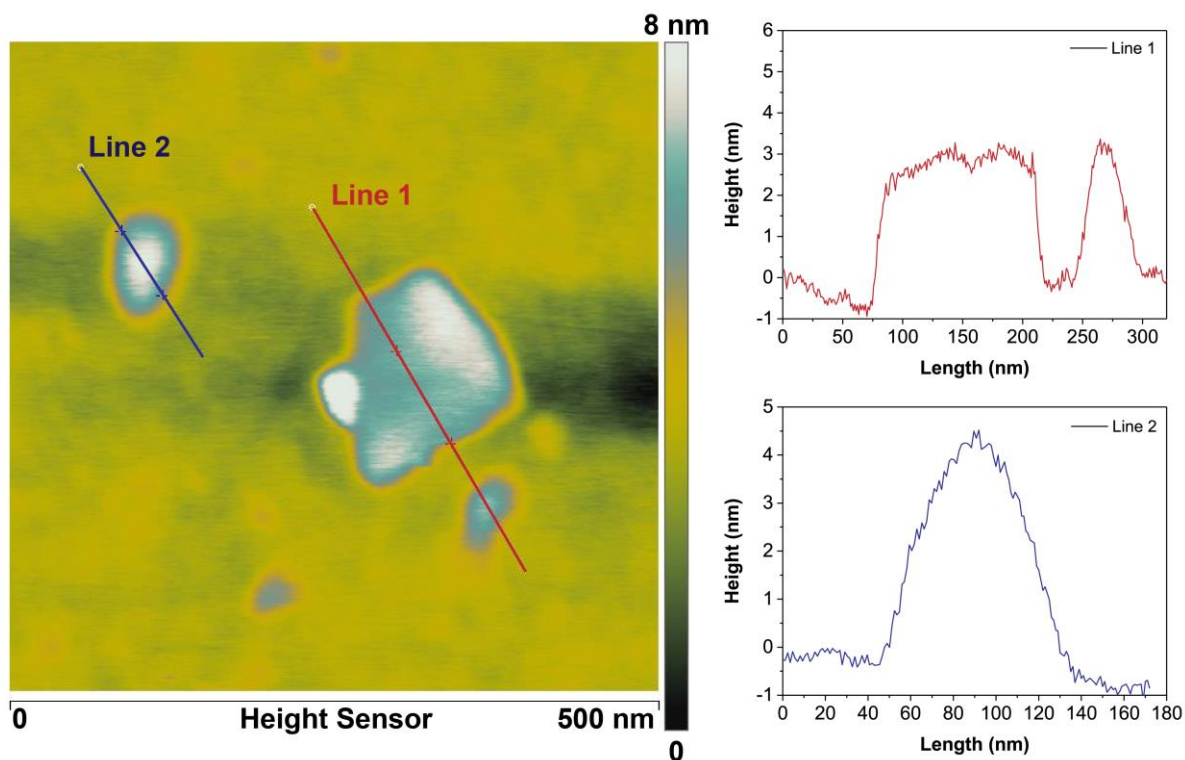
Figure S7. AFM images of cobalt-modified δ-MnO$_2$ and linear analysis of height profiles. Related to Figure 3.
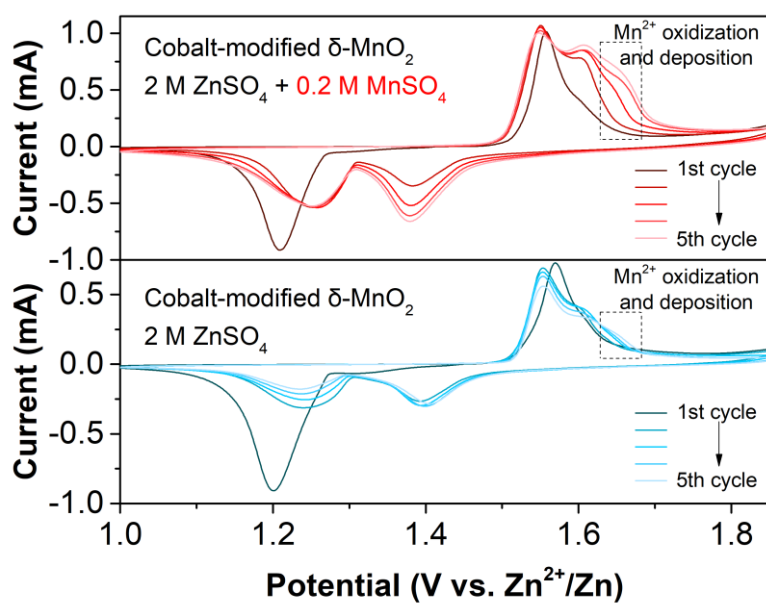
Figure S8. Comparison of CVs of coin-type batteries using Cobalt-modified δ-MnO$_2$ cathode in the electrolyte with or without additive MnSO$_4$. Related to Figure 4A.
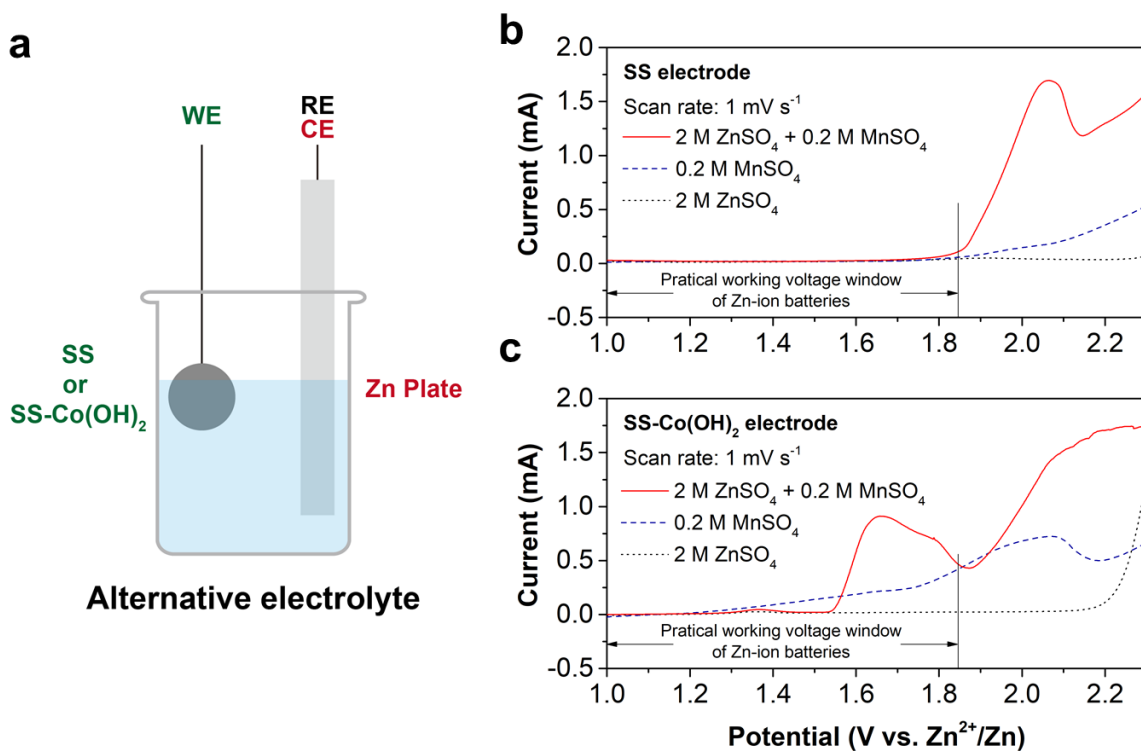
Figure S9. a) Illustration of the configuration of the home-made electrolyzer; Comparison of LSV profiles (positive sweep, 1 mV s^{-1}) of b) the SS electrode and c) the SS-Co(OH)$_2$ electrode in different electrolytes. Alternative electrolytes were utilized for evaluating the function of components in the electrolyte. The electrolyte used in this work included: 2 M ZnSO$_4$, 0.2 M MnSO$_4$, and 2 M ZnSO$_4$ + 0.2 M MnSO$_4$. Related to Figure 4B-E.
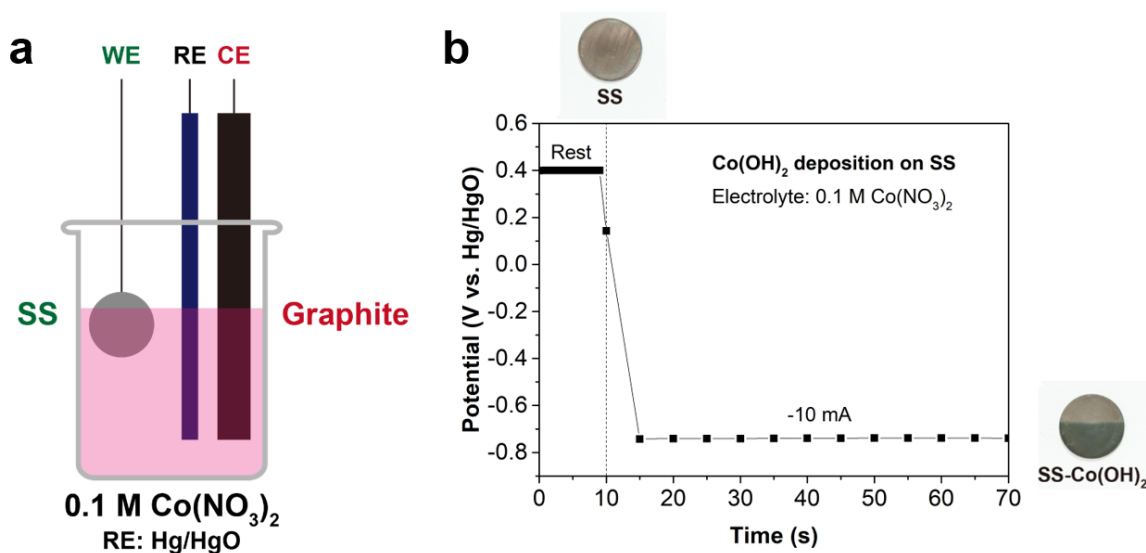

Figure S10. a) Illustration of the experimental setup for the electrodeposition of Co(OH)$_2$ on the SS electrode; and b) Potential response over time during the electrodeposition of Co(OH)$_2$ on the SS electrode for 60 s under a constant current of -10 mA with 0.1 M Co(NO$_3$)$_2$ as the electrolyte, Hg/HgO as the reference electrode and graphite as the counter electrode. Related to Figure 4B-E.
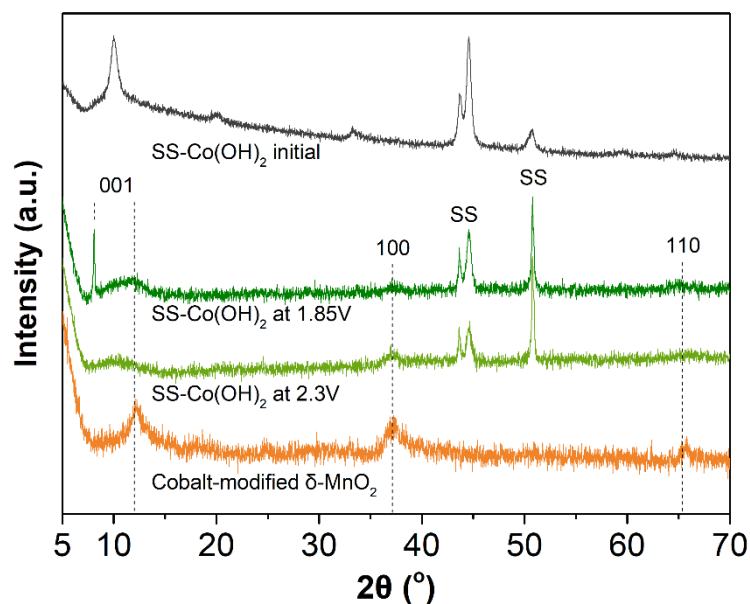
Figure S11. XRD profiles of the SS-Co(OH)$_2$ electrode at the initial state and after the LSV scan to 1.85 V and 2.3 V. Noted that to obtain a greater amount of the materials for identical XRD signal, the pre-deposition time of the Co(OH)$_2$ was tripled (180 s), and slower LSV scan rate was utilized (0.2 mV s^{-1}). The XRD profile of the cobalt-modified δ-MnO$_2$ powder sample is also presented for comparison. Related to Figure 4B-D.
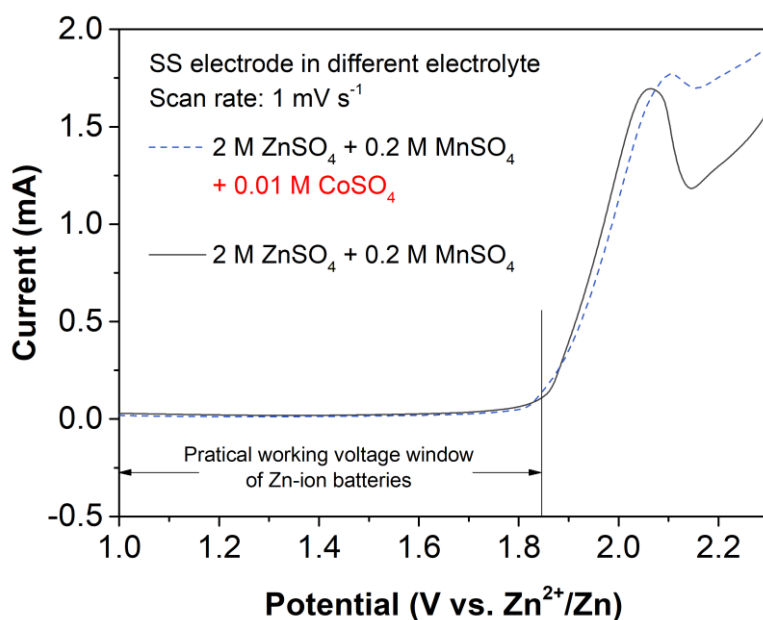

Figure S12. Comparison of LSV profiles (positive sweep, 1 mV s^{-1}) of a stainless steel (SS) in 2M ZnSO$_4$ + 0.2M MnSO$_4$ electrolytes with or without additional 0.01M CoSO$_4$. With a similar onset potential of ~1.9 V, this result indicates that the Co element in the state of unbound Co^{2+} in the electrolyte does not facilitate the deposition of active Mn compound. Related to Figure 4.
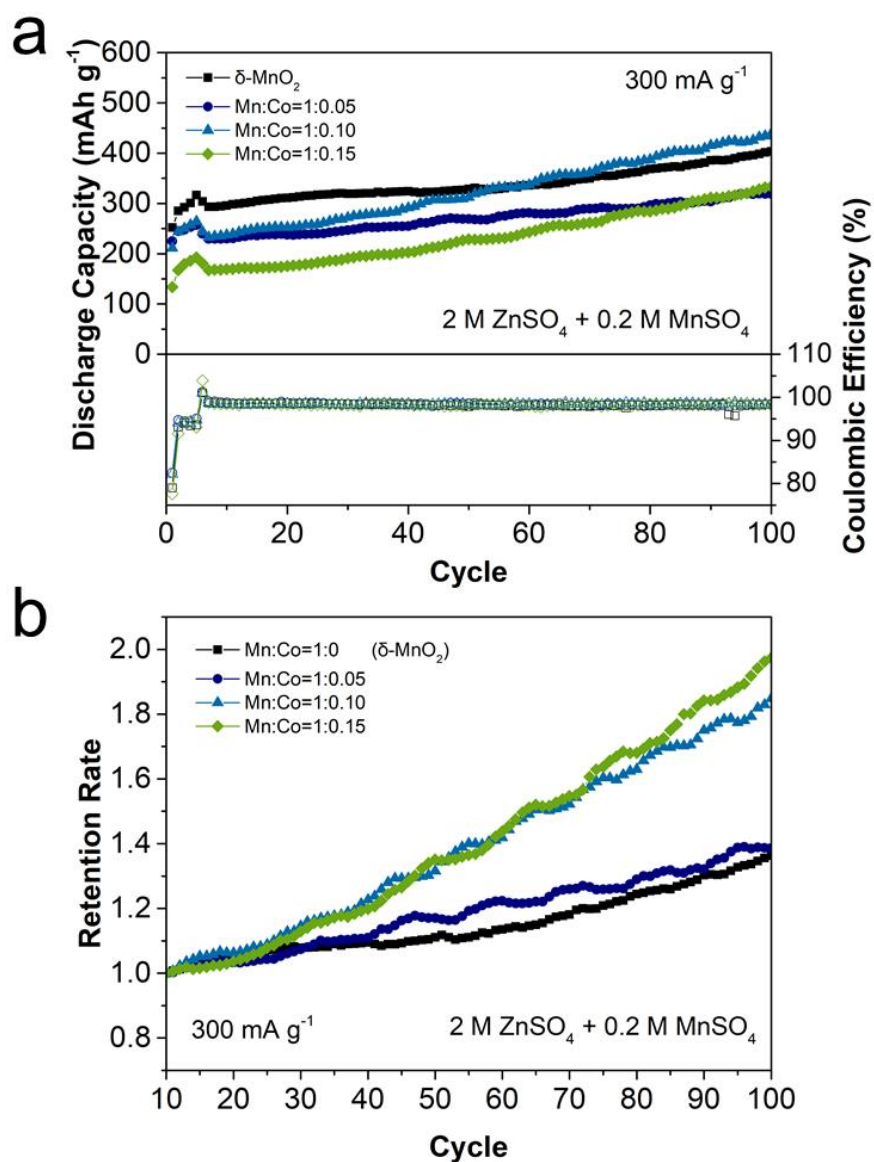
Figure S13. a) Comparison of cycling performance of manganese oxide cathodes with different contents of cobalt (See *Synthesis of manganese oxide with different cobalt contents* in **Transparent Methods**) using a 2 M $ZnSO_4$ electrolyte containing 0.2 M $MnSO_4$, b) Comparison of retention rates (the calculation of retention rate is based on the 10th discharging of the cathodes). Related to Figure 4.
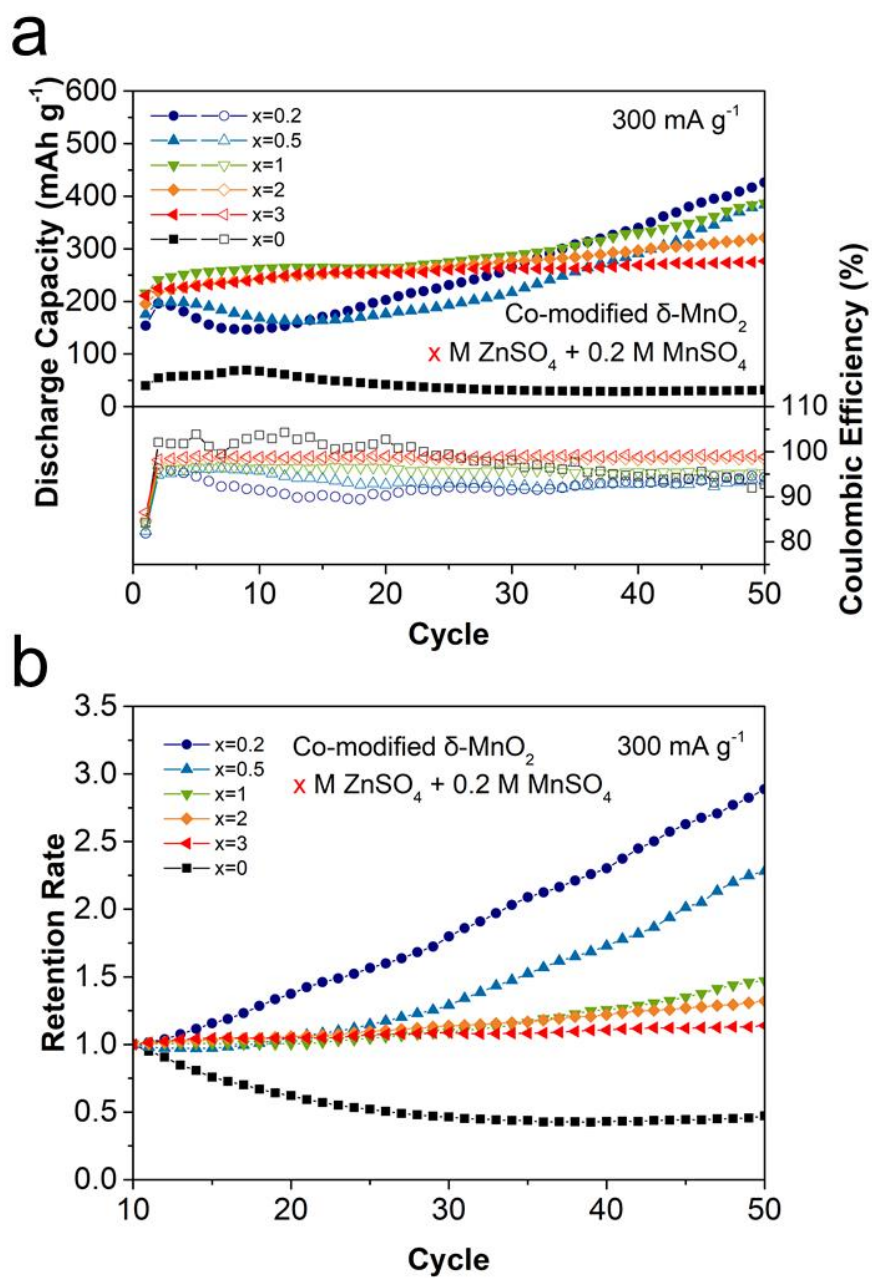
Figure S14. a) Comparison of cycling performance of cobalt-modified δ-MnO$_2$ cathode using electrolytes with different ZnSO$_4$ concentrations (x M) and a same MnSO$_4$ concentration (0.2 M), b) Comparison of the retention rates (the calculation of retention rates is based on the 10th discharging of the cathodes). Related to Figure 4.
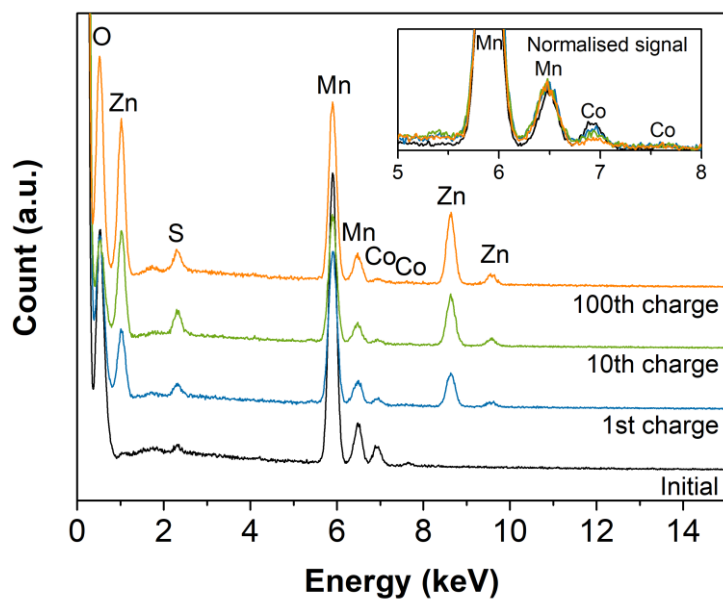
Figure S15. EDX profiles of the surface of cobalt-modified δ-MnO$_2$ cathode before cycling and after specific cycles at fully charged state (1.85 V). The inset shows the normalized signals where the Mn peak values at 5.9 keV were referred to as the maximum and the baselines as the minimum. Related to Figure 5.
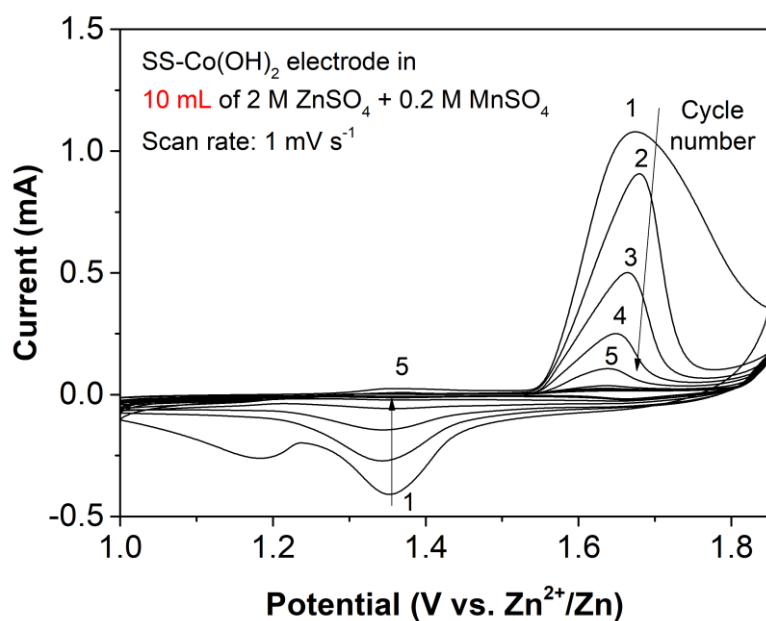

Figure S16. The first 10 CV cycles (1 mV s^{-1}) of SS with pre-electrodeposited Co(OH)$_2$. With a large volume (10 mL) of electrolyte, the Co(OH)$_2$ is gradually dissolved. The unbound Co^{2+} in the electrolyte does not facilitate the deposition of active Mn compound. Related to Figure 4E.
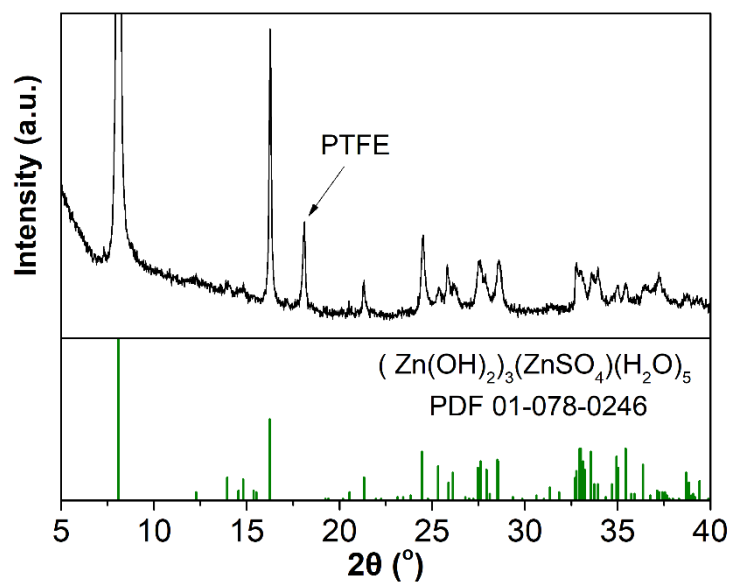
Figure S17. XRD profile of the cobalt-modified δ-MnO$_2$ cathode after first discharge to 1.0 V. Related to Figure 6.
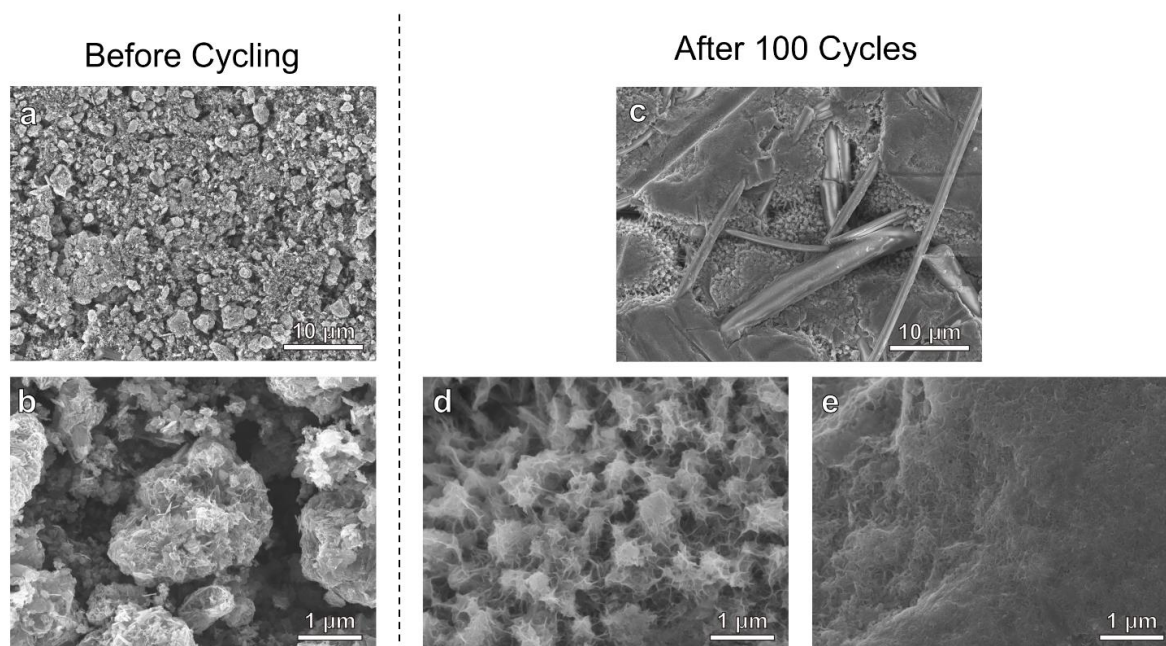

Figure S18. Morphology evolution observed with SEM images of cobalt-modified δ-MnO$_2$ cathode (conductive carbon and binder contained) a-b) before cycling and c-e) after 100 cycles. Related to Figure 6.
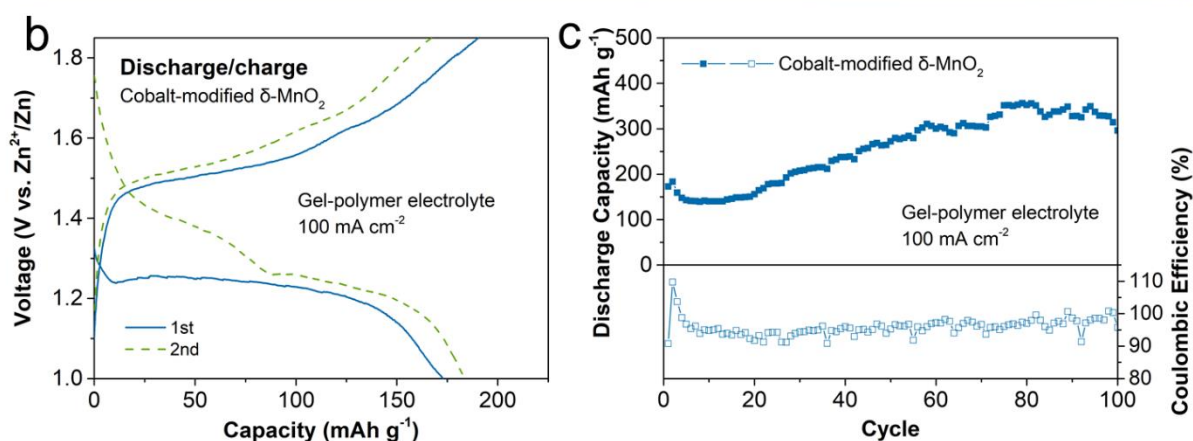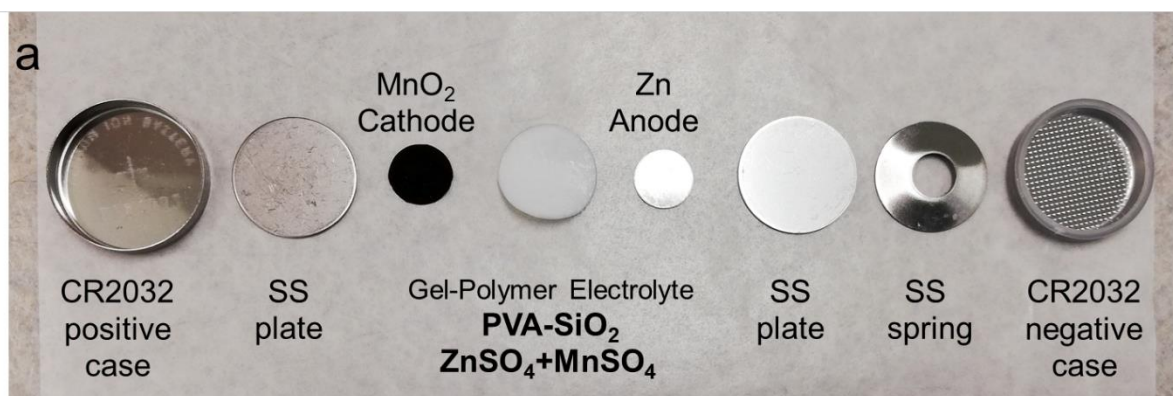
Figure S19. a) Components of a coin-type Zn-ion battery with a gel-polymer electrolyte (PVA-SiO₂); b) First and second discharge-charge profiles and c) Cycling discharge capacity and the corresponding Coulumbic efficiency over 100 cycles of a battery with the cobalt-modified δ-MnO₂ cathode and the gel-polymer electrolyte. Related to Figure 7.

Table S1. ICP-OES analysis of δ-MnO₂ and cobalt-modified δ-MnO₂. Related to Figure 2.

Sample	Na:Mn (at:at)	Co:Mn (at:at)
δ-MnO₂	0.074	/
Cobalt-modified δ-MnO₂	0.024	0.063

Note: all ratio results are averaged values based on three repeated samples with the same synthesis procedure.

Table S2. XPS analysis of δ-MnO₂ and cobalt-modified δ-MnO₂. Related to Figure 2B.

Sample	Na (at%)	Co (at%)	Mn (at%)	O (at%)	Na:Mn (at:at)	Co:Mn (at:at)
δ-MnO₂	1.01	/	26.90	72.08	0.038	/
Cobalt-modified δ-MnO₂	0.31	1.38	26.65	71.66	0.012	0.052

Transparent Methods

Synthesis of δ-MnO$_2$ nanosheets and α-MnO$_2$ nanowires

A molten-salt assisted synthesis procedure reported by Hu et al. (Hu et al., 2017) was adjusted in this work for a 10-minute fast synthesis of δ-MnO$_2$ nanosheets. Typically, 15 g of NaNO$_3$ and 0.6 g of MnSO$_4$·H$_2$O were mixed and ground with mortar to obtain a light pink fine powder. The powder was placed in a 150-mL crucible and heated at 350 °C for 10 min with a heating rate of 10 °C min^{-1}. After the synthesis, the crucible was immediately removed from the furnace at 350 °C and rapidly cooled down to room temperature. 100 mL of deionized (DI) water was added into the crucible and the liquid mixture was continuously stirred for 30 min at room temperature to dissolve the sintered NaNO$_3$ salt, then the mixture was filtrated. This washing procedure was repeated several times to completely remove the residual salt. After drying in an oven at 60 °C, the δ-MnO$_2$ product was obtained.

α-MnO$_2$ nanowires were synthesized via a hydrothermal method.(Pan et al., 2016) Herein, 0.51 g of MnSO$_4$·H$_2$O was dissolved in 90 mL of DI water, then 54.3 μL of 98% sulfuric acid was added into the solution. After that, another solution containing 0.32 g of KMnO$_4$ and 20 mL of DI water was mixed with the as-prepared acidic MnSO$_4$ solution. The mixture was then stirred in a beaker for 1 h and then put into an ultrasonic bath for another 30 min. The mixture was transferred to two 100-mL Teflon lined hydrothermal autoclaves and was heated at 120 °C for 16 h. After the hydrothermal autoclaves were cooled to room temperature, the obtained mixture was vacuum filtered and washed with DI water several times. After drying in an oven at 60 °C, the α-MnO$_2$ was obtained.

Synthesis of cobalt-modified δ-MnO$_2$

Typically, 0.2 g of as-prepared δ-MnO$_2$ powder was mixed with a 20 mL of 1 M CoCl$_2$ aqueous solution by constant stirring for 8 h at room temperature. The mixture was filtrated, and the as-obtained powder was further stirred with a new 20 mL of 1 M CoCl$_2$ for another 16 h. Then the mixture was filtrated and washed by DI water three times to remove the residual CoCl$_2$. After drying in an oven at 60 °C, cobalt-modified δ-MnO$_2$ powder was obtained.

Material characterizations

Chemical composition of the materials was qualitatively observed by energy-dispersive X-ray spectroscopy (EDX, Titan G2) and was further quantitatively evaluated with inductively coupled plasma-optical emission spectrometry (ICP-OES). Morphologies of the materials were observed using scanning electron microscopy (SEM) and transmission electron microscopy (TEM, Titan G2). Crystal phase structures of the materials were characterized with a combined analysis of X-ray diffraction (XRD, Bruker D8 Advance, Cu Kα radiation), high-resolution TEM (HR-TEM, Titan G2) and selected area electron diffraction (SAED, Titan G2). The thickness of the cobalt-modified δ-MnO$_2$ nanosheets was evaluated by TEM and confirmed by atomic force microscopy (AFM, Bruker Dimension Icon, platinum tip). Porosity and pore structure information was obtained with nitrogen adsorption/desorption (Micromeritics TriStar) at 77 K. Specific surface areas (S$_{BET}$) were evaluated using the Brunauer–Emmett–Teller (BET) theory. Total pore volumes were calculated with nitrogen uptake at p/p^0 = 0.99. Pore size distributions were calculated using Quenched Solid-State Functional Theory (QSDFT). Surface chemical states of the materials were analyzed with X-ray photoelectron spectroscopy (XPS, Kratos AXIS Ultra DLD, Al Kα radiation) and near-edge X-ray absorption fine-structure spectroscopy (NEXAFS, Australian Synchrotron(Cowie et al., 2010; Gann et al., 2016) in total electron yield (TEY) mode.

Electrochemical tests

Free-standing cathode film composed of cathode materials, conductive carbon (acetylene black) and polytetrafluoroethylene (PTFE) with a weight ratio of 7:2:1 were prepared for electrochemical performance tests. Typically, 0.07 g of MnO_2, 0.02 g of acetylene black, 1.67 g of 0.6 wt% PTFE (in ethanol solution) and 5 mL of absolute ethanol were mixed in a 30-mL bottle for 1 h using an ultrasonic bath. After drying the mixture at 60 °C in an oven, the dry powder was collected and wetted with ~500 uL of absolute ethanol, forming a soft black gum. The gum was ground with a glass bar and then peeled off and dried at 60 °C in a vacuum oven for ~12 h. Dried film disks with a diameter of ϕ 8 mm (area: 0.5 cm^2, areal loading of MnO_2: ~2.0 mg cm^{-2}) were cut using a hole puncher. Batteries were assembled as the order of a CR2032 positive case, a ϕ 16 mm stainless steel, a cathode film, a Whatman GF/D glass fiber, electrolyte, a 10x10 mm Zn plate, a ϕ 16 mm stainless steel, a stainless-steel shrapnel and a CR2032 negative case. Aqueous electrolyte for the Zn-ion batteries and for electrochemical deposition experiment on stainless steel was 2 M $ZnSO_4$ and 0.2 M $MnSO_4$ in DI water unless otherwise specified. Electrolyte volume used in each battery was 200 μL unless otherwise specified. Galvanostatic discharge-charge profile of the batteries was recorded using LANHE CT2001A battery test system (5 V, 10 mA). The specific current densities and specific capacities were calculated based on the weight of MnO_2 in the cathodes unless otherwise specified. Cyclic voltammetry (CV) profiles of the batteries and linear sweep voltammetry (LSV) of the electrochemical deposition of active Mn compound were obtained using a Biologic VSP potentiostat system.

Synthesis of manganese oxide with different cobalt contents

To evaluate the influence of cobalt content on the deposition of Mn compound and the electrochemical performance of the cathode, three manganese oxide materials with different cobalt contents were synthesized. For better control over the cobalt content, additional cobalt source ($CoSO_4 \cdot 7H_2O$) (with cobalt amounts of 0.05, 0.10 and 0.15 vs the atomic amount of Mn) was directly introduced in the same time with the manganese source ($MnSO_4 \cdot H_2O$) during the molten-salt synthesis process. For example, the sample with a Co:Mn=0.10:1 was synthesized by mixing 15 g of $NaNO_3$, 0.60 g of $MnSO_4 \cdot H_2O$ and 0.10 g of $CoSO_4 \cdot 7H_2O$ with mortar. Then the following procedure was same to the synthesis of δ-MnO_2. The sample obtained was denoted as Co:Mn=0.10:1 as shown in **Figure S13**.

Preparation of the gel-polymer electrolyte

25 g of DI water and 2.5 g of polyvinyl alcohol (PVA) were mixed by continually stirring with a magnetic stirrer at 100 °C. After the dissolution of PVA after ~3 h, 0.83 g of SiO_2 dispersion (containing 0.25 g of nano SiO_2) was added into the mixture and was mixed for another 1 h. The mixture was cooled to room temperature. The mixture liquid was cast into a stainless steel CR2016 battery positive case and put into a -20 °C fridge for 24 h. Then the freezing mixture was unfrozen. Two more times of the freezing and unfreezing were conducted until the electrolyte film became flexible and stretchable. The as-prepared film was soaked into a 2 M $ZnSO_4$ + 0.2 M $MnSO_4$ solution for 1 h. The film was removed from the solution and ready to be used as a gel-polymer electrolyte for a Zn-ion battery.